UNIVERSITY OF HELSINKI REPORT SERIES IN PHYSICS

HU-P-D244

Atom-level growth mechanism of nanoparticles by magnetron sputtering inert gas condensation

Junlei Zhao

Division of Materials Physics

Department of Physics

Faculty of Science

University of Helsinki
Helsinki, Finland

ACADEMIC DISSERTATION

To be presented, with the permission of the Faculty of Science of the University of Helsinki, for public criticism in auditorium XIV of the Main Building of the University of Helsinki, on November 12th 2016, at 12 o'clock noon.

HELSINKI 2016

ISBN 978-951-51-2226-1 (printed version)
ISSN 0356-0961
Helsinki 2016
Unigrafia Print

ISBN 978-951-51-2227-8 (PDF version)
http://ethesis.helsinki.fi
Helsinki 2016
Electronic Publications @ University of Helsinki

Junlei Zhao, **Atom-level growth mechanism of nanoparticles by magnetron sputtering inert gas condensation**, University of Helsinki, 2016, 59 p. + appendices, University of Helsinki Report Series in Physics, HU-P-D244, ISSN 0356-0961, ISBN 978-951-51-2226-1 (printed version), ISBN 978-951-51-2227-8 (PDF version)

Abstract

"There's Plenty of Room at the Bottom.", the lecture by Prof. Richard Feynman on December, 29th, 1959 at Caltech, USA, describes the field, which is "not quite the same as the others in that it will not tell us much of fundamental physics but it is more like solid-state physics in the sense that it might tell us much of great interest about the strange phenomena that occur in complex situations." This simple inspiring idea has often been referred to as the first "seed" of one of the most promising interdisciplinary branches of science, nanoscience.

Nanoparticles (NPs), one of the primary building blocks for nanostructures and its application, have been incidentally synthesized and used by ancient Romans when manufacturing beautiful cups. Modern technology requires the synthesis of NPs to be precise for specific application. The composition, structure, morphology and size are four parameters which dominate the properties of NPs. How to develop a method which can control these parameters accurately and precisely is an essential question for the researchers of nanoscience.

Among the wide range of existing synthesis methods, magnetron sputtering inert gas condensation has been commonly used during recent years. The method allows simultaneous control of composition, magnetron power, inert gas pressure, NP drift velocity, and aggregation zone length. To achieve a reliable control of the fabricated NPs, it is essential to understand how the nano-scale growth is influenced by these experimental conditions.

In this thesis, the growth mechanisms of Si, NiCr and Fe nanoparticles are studied using multi-scale simulation methods. We investigate the effects of the macro-scaled experimental parameters on the structural properties of nanoparticles. The work presented here is a step towards the understanding of the growth process of NPs in inert gas condensation chambers and the precise control of NP properties.

Contents

Abstract **I**

Contents **II**

1 Introduction **1**

2 Purpose and Structure **3**

2.1 Summaries of the original publications 3

2.2 Author's contribution 5

3 Nanoparticle **6**

3.1 Structure 6

3.2 Growth 9

4 Methods **11**

4.1 Magnetron Sputtering 11

4.2 Molecular Dynamics simulations 13

4.2.1 Basics 13

4.2.2 Interatomic Potentials 16

4.2.3 Simulation of nanoparticle growth by MD 18

4.3 Monte Carlo simulations 20

4.3.1 Metropolis Monte Carlo 20

4.3.2 Atomic Kinetics Monte Carlo 21

4.4 Finite Element Method 22

5 Atom-level growth mechanism of nanoparticles **26**

5.1 Formation of crystal Si nanoparticles 26

5.2 Surface segregation of NiCr nanoparticle 30

5.3 Formation mechanism of Fe nanocube 35

5.4 Bimodal distribution of Fe nanocube 43

6 Conclusions **47**

Acknowledgements **49**

Bibliography **51**

Chapter 1

Introduction

Nanoparticles (NPs), by definition, are particles of any shape with dimensions in the 1 to 100 nm range [1]. As functional building blocks, NPs occupy a very important place in various areas of nanoscience and biotechnology. NPs exhibit size-, shape-, composition- and structure-dependent behavior which is different from the corresponding bulk materials. By tuning these parameters, many properties, such as melting temperature, band gap (electronic structure), catalytic, magnetic and optical properties, can by controlled to meet the requirements of specific applications.

All these fascinating properties and applications of NPs rely on a simple fact: NPs have a very high surface/volume ratio. The surface plays a dominant role in defining their geometric and electronic structures. As stated by Wolfgang Pauli in 1991, "*God made the bulk; surfaces were invented by the devil.*"[2] Surfaces have unique behavior not observed in the bulk materials, such as faceting, relaxation and reconstruction. All these processes have been extensively studied in a branch of materials physics, so-called surface science. In this thesis, we will focus on NPs, a 3-D surface system, whose structures are usually determined by the symmetrical facets, edges and vertices. This will be discussed in detail in Chapter 3, Section 3.1.

The research on NPs usually concerns two steps: synthesis and characterization. Characterization methods often used in literature, include transmission electron microscopy (TEM), X-ray photoelectron spectroscopy (XPS) and so on. Synthesis methods can be roughly classified into two main approaches, chemical and physical, which are also referred to as liquid and gas phase growth, respectively. The chemical approaches usually involve a solution, which con-

tains certain metallic ions (*e.g.*, Ag^{+} and Fe^{2+}) and a reducing solvent [3–5]. The reduced metallic atoms slowly nucleate and condense into colloidal NPs. The physical methods [6–8] use pulsed laser, ion sputtering or thermal evaporation to create supersaturated vapor of certain species (*e.g.*, metals and semiconductors). NPs nucleate and grow in the gas phase, and finally are deposited on substrates. The physical paths will be discussed in detail in Chapter 3, Section 3.2.

The focus of this thesis are the theoretical and simulation issues in the nanoscience dealing mostly with synthesis of NPs via the gas phase condensation. The interplay among experiments, theory and simulations is very active. As stated by L. D. Marks in 1994, "*small particle structures cannot be understood purely from experimental data, and it is necessary to simultaneously use theoretical or other modeling.*" [9] The simulation techniques frequently used to study NPs are molecular dynamics (MD), kinetic Monte Carlo (KMC), Metropolis Monte Carlo (MMC) and density functional theory (DFT). Each method has a suitable time span and system size, which allows to focus on properties of interest. The detailed algorithm of each method will be described in Chapter 4.

In the work presented in this thesis, we study two different formation modes which are "Freezing of liquid nanodroplets" and "Solid-state growth" [10]. The former mode considers that the NP grows in a liquid phase and solidifies after its growth is completed. The final structure of the NP depends on the cooling process rather than the kinetics of the growth process. The simulation is done by cooling a free-standing NP, from the melting point or beyond, to room temperature. The temperature of NP is scaled either by conventional thermostats (publication **II**) or surrounding gas atmosphere (publication **I**). The second model is suitable for relatively low growth temperatures when the NP grows in solid phase. The final structure of NP is determined by the growth process. The simulation is done by adding atoms to a small initial NP at constant temperature (publication **III**). There are other possible formation modes such as collision and coalescence of NPs, but they are not discussed in this thesis.

Chapter 2

Purpose and Structure

The main purpose of this thesis is to provide a better understanding of the formation mechanism of the NPs during the magnetron sputtering condensation in inert gas atmosphere. The MD, MMC, KMC, FEM and analytical methods were used, since the studied processes such as phase transition, surface segregation, surface diffusion and oxidation, occur on very different time scales. In order to understand the full process of the growth of the NPs, one needs to combine different methods at the same time.

This thesis is based on four publications; they are referred to by bold-face Roman numerals. The structure of the thesis is as follows. In the following section, the four publications are summarized and the author's contribution is explained. Chapter 4 contains a general overview of the main computational methods used in this thesis: the classical MD, the classical Metropolis and kinetic Monte Carlo. Finally, in Chapter 5 the major results of this thesis are summarized and discussed.

2.1 Summaries of the original publications

Publication I: Crystallization of silicon nanoclusters with inert gas temperature control

J. Zhao, V. Singh, P. Grammatikopoulos, C. Cassidy, K. Aranishi, M. Sowwan, K. Nordlund, and F. Djurabekova, *Physical Review B* **91**, 035419 (2015)

We analyze the fundamental process of crystallization of silicon nanoclusters by

means of molecular dynamics simulations, complemented by magnetron-sputter inert gas condensation, which was used to synthesize polycrystalline silicon nanoclusters with good size control. Both the simulations and experiments show that upon cooling down by an Ar gas thermal bath, initially liquid, free-standing Si nanocluster can grow multiple crystal nuclei, which drive their transition into polycrystalline solid nanoclusters.

Publication II: Surface segregation in Chromium-doped NiCr alloy nanoparticles and its effect on their magnetic behavior

M. Bohra, P. Grammatikopoulos, R. E. Diaz, V. Singh, J. Zhao, J.-F. Bobo, A. Kuronen, F. Djurabekova, K. Nordlund, and M. Sowwan, *Chemistry of Materials* **27(9)**, pp 3216-3225 (2015)

In this study, we demonstrate the element-specific Cr segregation in Ni-rich NiCr alloy nanoparticles and nanogranular films grown by gas-phase synthesis methods. In situ annealing measurements (300–800 K), performed under vacuum using aberration-corrected environmental transmission electron microscopy (E-TEM), and vibrating sample magnetometry (VSM) revealed progressive Cr segregation with annealing temperature and subsequent complete transformation into core–satellite structures at 700 K. Simultaneously, atomistic computer simulations (molecular dynamics (MD) and Metropolis Monte Carlo (MMC)) elucidated the resultant structures, explaining the driving force behind the segregation energetically.

Publication III: Formation mechanism of Fe nanocubes by magnetron sputtering inert gas condensation

J. Zhao, E. Baibuz, J. Vernieres, P. Grammatikopoulos, V. Jansson, M. Nagel, S. Steinhauer, M. Sowwan, A. Kuronen, K. Nordlund and F. Djurabekova, *ACS Nano* **10(4)**, pp 4684–4694 (2016)

In this work, we study the formation mechanisms of iron nanoparticles (Fe NPs) grown by magnetron sputtering inert gas condensation and emphasize the decisive

kinetics effects that give rise specifically to cubic morphologies. Our experimental results, as well as computer simulations carried out by two different methods, indicate that the cubic shape of Fe NPs is explained by basic differences in the kinetic growth modes of $\{100\}$ and $\{110\}$ surfaces rather than surface formation energetics. Both our experimental and theoretical investigations show that the final shape is defined by the combination of the condensation temperature and the rate of atomic deposition onto the growing nanocluster.

Publication IV: Chemoresistive gas sensors based on magnetron sputtered iron nanocubes

J. Vernieres, S. Steinhauer, J. Zhao, A. Chapelle, P. Menini, R. E. Diaz, K. Nordlund, F. Djurabekova, P. Grammatikopoulos and M. Sowwan, *ACS Nano* Submitted

Preprinted with permission in the printed version of this thesis.

In this work, we demonstrate precise size and shape control during formation of Fe nanocubes, introducing the ferromagnetic target thickness as a decisive experimental parameter. We obtain a yield increase of one order of magnitude compared to experiments using mass filtration. This enables the fabrication of chemoresistive gas sensor devices with excellent performance for NO_2 detection down to 3 ppb, due to the nanoparticles' specific hollow-nanocube morphologies. Our results can lead to future large-scale production of nanosensors integrated with standard microelectronic components.

2.2 Author's contribution

The author carried out all the MD simulations for publications **I** and **III**, performed the analysis of the results of those simulations and developed the analytical model. For publication **II**, the author carried out the MMC simulations and performed atomic stress analysis of the results. For publication **IV**, the author carried out the FEM and sputtering yield simulations, and developed the analytical model of the growth of the nanoparticles.

The author wrote the corresponding part of the computational simulations and described the analysis of the obtained results and participated in the discussion of all the results.

Chapter 3

Nanoparticle

3.1 Structure

In this section, we review the studies on the structure of NPs. As briefly mentioned in Chapter 1, NPs have structural properties different from their bulk counterparts because of the large fraction of surface atoms. This difference can be seen both in physical and chemical aspects. In solid phase, the structure of NP can be defined as amorphous, quasi-crystal, polycrystal and single crystal. The most favored structure is the one with the minimal total energy. Although the ground state is not always reached in the experiments (because of kinetic effects discussed in Section 3.2), it is an ideal starting point to understand the physics in NP science.

The simplest structure of NPs is a spherical "ball" cut out of the bulk material. It is known that a sphere has the minimum surface for a given volume, which should lead to the ground state based on a simple equation:

$$E_{tot} = V \cdot E_{bulk} + A \cdot \gamma_{surf} \tag{3.1}$$

where E_{tot} is the total potential energy, E_{bulk} is the cohesive energy per unit volume, γ_{surf} is the surface energy per unit area ,and V and A are volume and surface area of the NP, respectively. With constant V, E_{bulk} and γ_{surf}, E_{tot} approaches the minimum value when A is minimized for a spherical shape. However, it is not always true, because usually γ_{surf} is defined by a specific crystallographic direction of the facet. The crystallographic direction describes how close the facet is packed and is described by a set of Miller indices h, k and l. To distinguish a surface energy of each facet, a common notation $\gamma_{(hkl)}$ is used. The total surface energy of a faceted

NP can then be written as:

$$G = \sum_i G_i = \sum_i \gamma_i A_i \tag{3.2}$$

where the i subscript represents a certain surface facet of area A_i.

The minimum energy shape for a given volume is determined by the minimization of the sum of the surface energies of all facets comprising the surface. The solution which is known as '*the Wulff construction*', was first proposed by Wulff [11] in 1901 and later proven by Herring [12] in 1953. The theorem states that the normal distance from a common center to any given surface facet is proportional to the surface free energy of that facet, as presented in Figure 3.1.

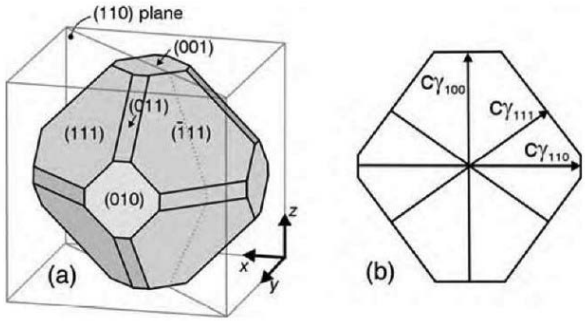

Figure 3.1: Schematic diagram of the Wulff construction. (a) Cluster displaying three types of facets. (b) Cross section of the cluster along the (110) plane.

Although the Wulff construction is the correct solution for large single crystal NPs, it does not always works with much smaller ones. Because of the discrete nature of atoms, the surface atoms do not have the identical free energy. The numbers of *edge* and *vertex* atoms with higher free energy become significant for small NPs. This will lead to a large deviation from the Wulff construction. Moreover, the assumption of perfect single crystal NPs is not valid for small ones, since internal stress will be induced in bulk to compensate the surface energy minimization. This will lead to the fact that many polycrystalline or noncrystalline structures are found to be the ground state of small NPs.

Here we show several typical examples of the ground states of small NPs [13]. Firstly, as shown in Figure 3.2(a) and (b), for FCC metals, the single crystal NPs form octahedron and truncated octahedron. The former one has eight close-packed (111) facets and the latter one has six more

square (100) facets at the original vertices. These two structures have the minimal internal stress, but relatively high surface/volume ratio, so they are usually seen in sufficiently large NPs. For smaller NPs, noncrystalline structures such as icosahedron and decahedron turn out to be more favorable. An icosahedron (Figure 3.2(c)) has 20 triangular distorted (111) facets. It can be considered as 20 fcc tetrahedra sharing a common vertex at the center or a 'onion-liked' sphere (with 1 atom at the center, 12 atoms in the second layer and so on). The whole structure is compressed within shells and stretched between shells. Another structure, a decahedron, has 10 (111) facets (Figure 3.2(d)). It can be regarded as five FCC tetrahedra sharing a common edge along the fivefold axis. Since the angle between the sides of a perfect tetrahedron is about 70.53 degree, the tetrahedra are slightly distorted. The regular decahedron is far away from a sphere, thus it has a higher surface/volume ratio. It can be improved by removing the five edges which are normal to the fivefold axis as shown in Figure 3.2(e). Even better solution were found by Marks [9], a further truncation of the outermost edge atoms (Figure 3.2(f)).

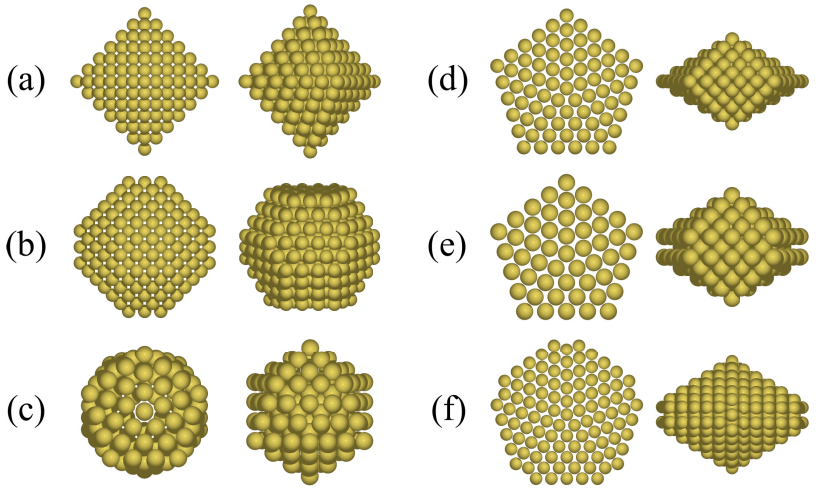

Figure 3.2: Examples of the possible ground states of NPs. (a) octahedron; (b) truncated octadedron; (c) Mackay icosahedron; (d) regular decahedra; (e) Inotruncated decahedra; (f) Marks truncated decahedra. Each cluster is shown in two views.

Overall, the icosahedron and decahedron are both under internal stress, so they should be the ground states only for small NPs. However, there are plenty of experimental reports showing that both shapes icosahedron and decahegron can be seen for fairly large size NPs (up to 20

nm) [14–17]. These observation clearly cannot be explained by energetics considerations, so kinetics of growth process should be taken into account.

3.2 Growth

As briefly mentioned in Chapter 1, the growth process of NPs was mainly studied in two models depending on temperature. The first one is the *liquid-state growth model* which means that the NP remains in a liquid phase while growing. In this model, the final structure of the NPs do not depend on the kinetics of landing of the deposited atoms, but rather depends on the cooling process afterwards. To simulate the process, the common way is to cool a certain size NP from a temperature above melting point to the solidified temperature where no more significant diffusion process can occur. The cooling rate is usually in the range of $10 - 10^{-2}$ K/ns. The cooling can be done by applying a thermostat directly to the NP or only to the atoms of the surrounding atmosphere. This will be discussed in detail in Section 4.2.3. The essential process determining the final structure of NPs is solidification. For most metals, the solidification refer to the process that liquid metal atoms crystallize into poly-crystalline, single crystalline phase or even rearrange into noncrystalline such as icosahedron and decahedron structure. For semiconductors such as silicon and germanium, the final structure can also be totally in amorphous phase (see publication **I**). The size, material and cooling rate of the NPs are the three key factors. Firstly, smaller NPs tend to end up in the most favorable structure more easily, since less atoms are involved and the liquid phase may not be far away from the ground state. Secondly, metals are very easy to crystallize. However, a semiconductor NP needs to be cooled down very slowly to reach the crystalline phase. Finally, because NP is a surface-abundant system, *supercooling* is commonly seen during the cooling process.

On the other hand, the second model is the *solid-state growth model*, as NPs grow at temperature well below the melting point. These simulations are originally done by adding atoms to a small initial nucleus at constant temperature [18, 19]. The surface atoms should be allowed to move freely to mimic the surface diffusion. The final outcome is a trade-off between the atomic deposition flux and the movement of the surface atoms. It is a random process for gas-phase atoms landing on a free-flying cluster. After landing, the adatoms will be trapped in local potential minima for relatively long time. The diffusion drives the system to the ground state in

the end, but the time scale will reach the laboratory time scale at room temperature due to the low mobility of the surface atoms.

Although the single-atom movement is relatively slow at low temperature, the solid-state transitions were seen in both experiments and simulations [20]. The previous researches on the kinetic growth of fcc metals have show that it is possible to grow a large icosahedra NP from a small decahedron seed, by creating an external incomplete icosahedral shell, and then letting the symmetry propagate to the inner [21]. These experiments and simulations were done at elevated temperature or under irradiation condition.

Chapter 4

Methods

4.1 Magnetron Sputtering

Among the many methods developed to produce NPs, magnetron sputtering is one of the gas-phase condensation methods which are mainly used at the laboratory level for basic research purpose. A high-vacuum magnetron-sputter inert-gas-phase NP source, as shown schematically in Figure 4.1, has been developed by Mantis Deposition ltd. recently. The system has four modules which are the cluster source and aggregation zone, shellcoater, quadrupole mass-filter (QMF), and main deposition chamber labelled A, B, C, and D, respectively.

In module A, a water-cooled aggregation chamber with a 2-inch in diameter magnetron sputtering target inside is used for vapor generation. The cluster source comprises a set of permanent magnets, an inert gas source, a copper cathode and the target. Ar or Ar/He mixed gas is heated up and ionized into the plasma. The Ar^+ ions are accelerated by the electric bias between the anode and the copper shield (the cathode), and bombard the target. The secondary electrons are confined by the magnetic field and significantly enhance the ionization of the Ar gas near the target surface. This way, more energetic Ar^+ ions bombard the target, generating super-saturated vapor for cluster nuclei formation.

The vapor is cooled by collisions with inert gas atoms and blackbody radiation. At the initial stage, the temperature of nuclei are initially beyond their melting points due to the bond forming energy, referred as "liquid growth" stage. Further growth occurs by more sputtered atoms landing on the nascent NPs, and subsequently by collisions and coalescence of the NPs. The

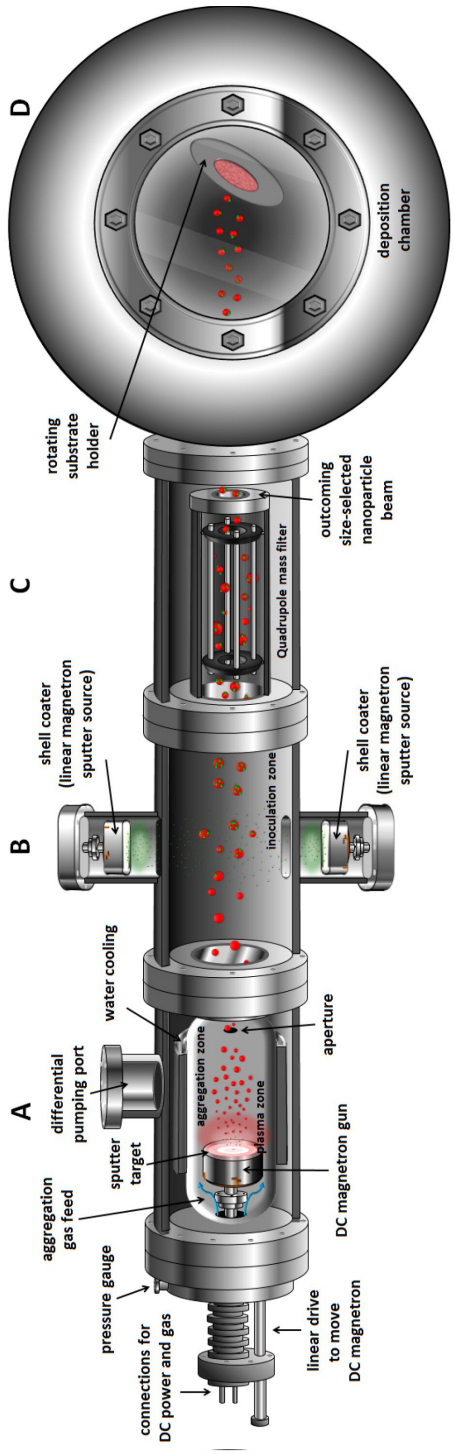

Figure 4.1: Schematic representation of a magnetron-sputter inert-gas condensation NP deposition system from Ref. [22].

temperature of NPs at this second stage is essential for the final properties of NPs, as it can be either "liquid growth" or "solid-state growth". After the NPs passing the source aperture, the growth finishes due to the long distance between each NPs. The optional further growth can be done in shell coater chamber (module B). Depending on the power of the coating source and residence time, the NPs can grow into core-shell, core-satellite or Janus structure [23, 24]. After passing through a quadrupole mass filter (module C), the NPs softly land on suitable substrate in the deposition chamber (module D). Embedded NPs can be achieved by applying an additional bias on the substrate.

The final outcome of the NPs is a result of thermodynamics and kinetics history during the aggregation, inoculation and deposition. It is a nontrivial work to fully understand the NP-growth mechanism in this system via computer simulation methods, since the existing experimental tools may not be sufficient to track atom motion in a multiphase system. Therefore, in this thesis, we use molecular dynamics, Metropolis Monte Carlo and kinetic Monte Carlo methods to study the atom-level growth mechanism of NPs.

4.2 Molecular Dynamics simulations

4.2.1 Basics

Molecular dynamics (MD) is a simulation method developed in the late 1950s by Alder and Wainwright [25, 26]. The idea is to solve Newton's equations of motion numerically for a many-body system. A simplified description of the MD algorithm is shown in Figure 4.2. The initial positions of the system $\mathbf{r_i}(t_0)$ should be given as an user input. The initial velocity of each atom $\mathbf{v_i}(t_0)$ can be generated from the Maxwell distribution corresponding to the initial temperature of the system. Then, all forces acting on each atom are calculated with a well defined interatomic potential $\mathbf{V}(r)$ (see Section 4.2.2). The positions and velocities will be updated by integrating the equations of motion numerically over a small time step Δt. Commonly used integration algorithms are velocity Verlet [27] and Gear5 [28].

In addition, it is important to choose the appropriate timestep Δt. If Δt is too large, the total energy of the system is not conserved, which will lead to a nonphysical result. If Δt is too small, the simulation become inefficient, as the computational power is wasted for giving

the same results as with the optimal timestep. In normal equilibrium state, 1-2 fs is usually sufficiently small to achieve the energy conservation. In non-equilibrium simulations (*e.g.*, irradiation cascade), a variable timestep is often used to maximize efficiency [29].

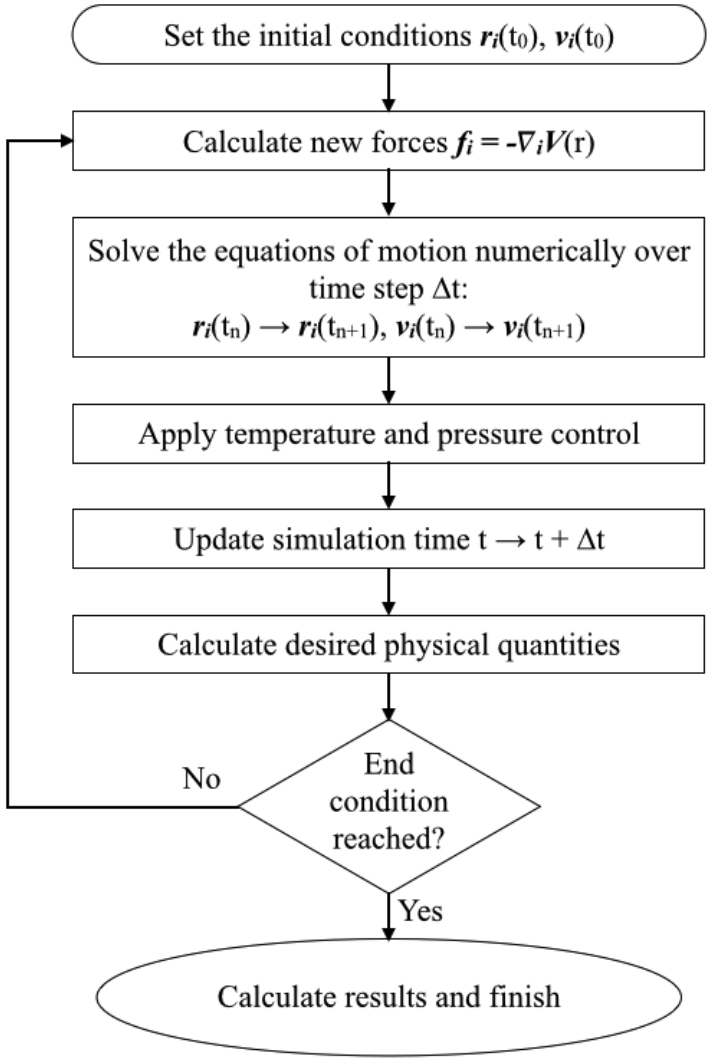

Figure 4.2: Basics steps of the MD algorithm.

The original MD is to simulate a system in micro-canonical ensemble (NVE). However, in real experimental conditions, a system usually exchanges energy with the surrounding environment

by changing temperature (T) and volume (V). If both T and V are kept as constants, the system presents a canonical ensemble (NVT). If T and P (pressure) are kept as constants, the system is in isothermal-isobaric ensemble (NPT). It is necessary to develop algorithms to mimic such conditions. These additional algorithms are called thermostats for controlling T and barostats for controlling V.

Two types of thermostats are used in this thesis. One simple and efficient thermostat was suggested by Berendsen et al. [30]. The temperature control is achieved by rescalling the velocities of atoms every time step with the factor:

$$\lambda = \sqrt{1 + \frac{\Delta t}{\tau_{\mathrm{T}}}(\frac{T_0}{T(t)} - 1)} \tag{4.1}$$

where T_0 is the desired temperature, τ_{T} is the time constant determining the scaling rate. The system temperature $T(t)$ will exponentially damp to the desired temperature:

$$\frac{T(t)}{dt} = \frac{T_0 - T(t)}{\tau_{\mathrm{T}}} \tag{4.2}$$

The Berendsen thermostat appears reasonably accurate and effectively converges to the desired temperature T_0. However, one disadvantage is that it does not preserve a canonical ensemble suppressing realistic (physical) temperature fluctuations. Specifically for simulations of nanoparticles in vacuum, the well-known *flying ice cube* effect [31] leads to totally nonphysical artifacts, so other methods are more commonly used in this thesis.

In contrast to Berendsen thermostat, extended system methods treat the heat bath as an imaginary reservoir which is coupled to the real system. One algorithm was originally introduced by Nosé [32] and subsequently improved by Hoover [33]. In the approach of Nosé, an additional generalized coordinate s, its conjugate momentum p_s and am imaginary mass Q are assigned to the heat bath. The Hamiltonian of the extended system is written as:

$$\mathcal{H} = \mathcal{K} + \mathcal{K}_s + \mathcal{U} + \mathcal{U}_s = \sum_i \frac{\mathbf{p}_i^2}{2m_i s^2} + \mathcal{U}(\mathbf{r}) + \frac{p_s^2}{2Q} + g k_B T \ln(s) \tag{4.3}$$

where g is the number of independent momentum degrees of freedom of the system. The equations of motion of the real system is written as:

$$\mathbf{v}_i = \dot{\mathbf{r}}_i = \frac{\partial \mathcal{H}}{\partial \mathbf{p}_i} = \frac{\mathbf{p}_i}{m_i s^2}; \quad \dot{\mathbf{p}}_i = -\frac{\partial \mathcal{H}}{\partial \mathbf{r}_i} = \mathbf{f}_i \tag{4.4}$$

The Nosé-Hoover thermostat gives a correct canonical ensemble (NVT), but also needs a long time for thermalization. In practice, a simulation often starts with the Berendsen thermostat to reach the desired temperature and then uses the Nosé-Hoover thermostat to probe a right canonical ensemble. Moreover, both methods can be applied either to the entire system, or just at certain regions of the simulation cell.

Barostats are rarely used in the thesis, but should be mentioned briefly. A similar scaling technique can be applied to control a pressure P in the system at the desired level P_0 by changing the system size and scaling the atomic coordinates in all three x, y, z dimensions simultaneously, or only along the selected directions. The scaling factor μ is defined as:

$$\mu = \sqrt[3]{1 - \frac{\beta \Delta t}{\tau_{\mathrm{P}}}(P_0 - P)} \tag{4.5}$$

where $\beta = 1/E_{\mathrm{bulk}}$ is the isothermal compressibility of the system, used solely to make the time constant τ_{P} independent on the simulated material. This method has also been suggested by Berendsen [30] and is therefore called the Berendsen pressure control. One should note that, similar to Berendsen thermostat, Berendsen barostat does not yield the proper ensemble. Extended system methods can be applied to pressure control, such as Andersen [34] and Parrinello-Rahman [35] barostat.

The MD codes used for this thesis are mainly PARCAS [36, 37] and LAMMPS [38] .

4.2.2 Interatomic Potentials

The reliability of classical MD simulations depends crucially on the semi-empirical potentials which are used to describe the interactions between atoms. A valid potential should reproduce several important physical properties of materials, *e.g.*, lattice constant, Young's modulus, melting point, defect formation energies and the ground-state phase. For nanoparticle growth in inert gas, a potential should work well for the equilibrium state over a wide range of temperatures. In this section, several commonly used potentials for semiconductors, pure metals and metal alloys are introduced.

Stillinger-Weber (SW) potential is a well established potential for semiconductors. It is first developed for silicon [39] and later on, it was parameterized for germanium [40, 41] and gallium nitride [42, 43]. The potential-energy function consists of a pair potential and an angular-dependent potential, as follows:

$$f_2(r_{ij}) = \begin{cases} A(Br_{ij}^{-p} - r_{ij}^{-q})exp[(r_{ij}-a)^{-1}] & r_{ij} < a \\ 0 & r_{ij} \geq a \end{cases} \tag{4.6}$$

$$f_3(\mathbf{r}_i, \mathbf{r}_j, \mathbf{r}_k) = h(r_{ij}, r_{ik}, \theta_{jik}) + h(r_{ji}, r_{jk}, \theta_{ijk}) + h(r_{ki}, r_{kj}, \theta_{jki}) \tag{4.7}$$

where θ_{jik} is the angle between atom j and k at vertex atom i and function h has the following form:

$$h(r_{ij}, r_{ik}, \theta_{jik}) = \lambda exp[\gamma(r_{ij}-a)^{-1} + \gamma(r_{ik}-a)^{-1}] \times (\cos\theta_{jik} + 1/3)^2 \tag{4.8}$$

The SW potential describes the crystalline, amorphous and liquid phases of silicon fairly well. It has been used in publication **I** to compare with the Tersoff potential of silicon.

Tersoff potential [44, 45] gives the bond energy between atoms i and j as:

$$V_{ij} = f_C(r_{ij})[f_R(r_{ij}) - b_{ij}f_A(r_{ij})] \tag{4.9}$$

where f_R is a two-body term, $b_{ij}f_A(r_{ij})$ is an angular-dependent term and f_C is a cutoff function. It describes the silicon crystal structure quite well, but it is found to overestimate the melting point of silicon significantly.

Embedded-atom method (EAM) is extensively used for metals [46–48] and metal alloys [49–51]. The basic format of the potential energy of an atom is written as:

$$E_i = \frac{1}{2}\sum_{i \neq j} \phi_{ij}(r_{ij}) + F_i(\sum_{i \neq j} \rho_j(r_{ij})) \tag{4.10}$$

where ϕ_{ij} is a pair-wise potential, ρ_j is the electron charge density from atom j at the location of atom i, and F_i is an embedding function which represents the energy required to place atom i into the electron cloud. The pair-potential term ϕ describes electrostatic contribution which is usually short-ranged and repulsive. In the original EAM, the electron density ρ is a uniform

function in all direction, but in the so-called modified EAM (MEAM) [52, 53], an angular dependence of the electron density function is introduced to account for the local symmetries in interatomic bonding. The embedding energy term F has various expressions derived from different physical properties. For example, *Sandia* EAM potentials developed by Foiles et al. [54] for FCC metals do not have an analytical form, but are given as a table of data points fitting to experimental data. Spline interpolation is used to evaluate the functions. Finnis-Sinclair potential [55, 56] has simple function forms $F_i(x) = -A\sqrt{x}$ and $\rho_j(r_{ij}) = (r_{ij} - d)^2$ for $r_{ij} \leqslant d$.

In publication **II**, a recent EAM potential for Ni-Cr-Fe alloy [46] is used. A Finnis-Sinclair potential developed by Mendelev et al. [57] for crystalline and liquid iron is used in publication **III** and **IV**. More attention need to be paid to the magnetic properties of transition mental elements, as Fe, Ni and Cr all exhibits interesting magnetic properties. In classic MD, the magnetic properties are normally included implicitly, since the potentials are fitted to cohesive energies, elastic modules and so on, which include the magnetic contribution. The explicit inclusion of magnetic moments should be calculated by the methods such as DFT and beyond, but the size scale of such methods is limited and inapplicable to the large system in this thesis.

4.2.3 Simulation of nanoparticle growth by MD

The previous MD studies on the free-standing NPs was mainly done by NVE ensemble or applying a thermostat at constant temperature. However, as discussed in Section 4.2.1, the algorithm of the velocity rescalling method fails to reproduce the correct linear and angular momentum of NPs. On the other hand, extended system methods give the correct NVT ensemble, but cannot distinguish the surface and bulk atoms in NPs. Therefore, for the study of nanoscale processes of NPs, special attention must be paid to how the simulations are conducted. For example, special thermo- and barostats are required to control the simulation conditions compared to the conventional ones used to study the bulk materials.

In publication **I** and **III**, we simulated the cooling process of NPs via a inert gas temperature control. A general setup of the simulations are shown in Figure 4.3. The pure NP in the liquid phase was initially placed in the center of the simulation cell. The surrounding atmosphere consisted of isolated Ar atoms, randomly distributed around the NP. The initial velocities of all

atoms were generated in a Maxwell-Boltzmann distribution to ensure a desired initial temperature in all simulations. In a common situation, the linear and angular momentum of NP and Ar gas is initially removed separately. The temperature of Ar atoms was constantly scaled to 300 K by thermostats, whence the temperature of the whole system was reduced via the thermal bath of the Ar atmosphere. The whole system can be regarded as a canonical (NVT) ensemble but far away from the equilibrium state. The cooling rate of the NP is determined by the collision rate between Ar atoms and NP surface. We can use an analytical equation to estimate the cooling rate:

$$\frac{dT_c(t)}{dt} = (T_c(0) - T_g)n_{co}(1 - \frac{k}{3nk_B})^{n_{co}t} \ln(1 - \frac{k}{3nk_B}) \tag{4.11}$$

where n_{co} is the collision rate, k is the energy exchange constant, n is the number of atoms in the NP, T_g is the temperature of the inert gas and k_B is the Boltzmann constant.

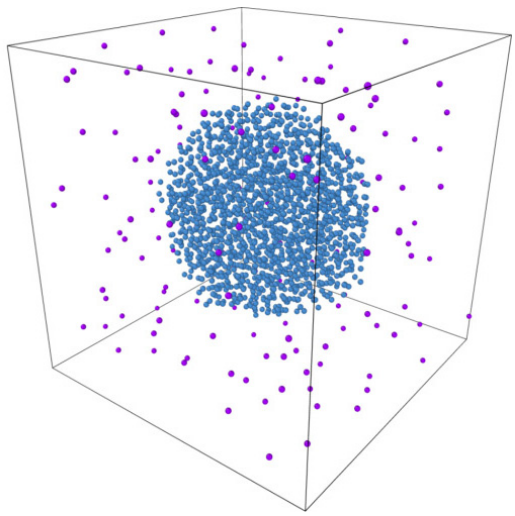

Figure 4.3: Typical setup of the MD simulation of the cooling process of NP with inert gas temperature control. A NP (blue atoms) in Ar atmosphere (red atoms) with periodic boundary condition.

In solid-state growth simulation of NPs, due to the weak coupling between the inert gas temperature control and the NP, one needs to use a very high ratio of Ar to NP atoms in the simulation

to achieve sufficient cooling. The reasonable ratio of the number of Ar to NP atoms is about 50 to 100, which will make the MD simulation extremely expensive due to the long simulation time. To simulate the solid-state growth process of NPs, we need the other setup. Initially, a spherical NP was placed in the center of the simulation cell. The ambient atmosphere consisted of isolated Fe atoms. The Nosé-Hoover thermostat was applied to the atoms initially located within the small spherical region at the center of the NP. The energy release duo to the deposition of atoms is dissipated by the thermostat. The deposition rate was simulated by adding a new NP atom. The advantage of this set up is that it can control the temperature of the NP within a desired range without controlling the thermal evolution of the surface atoms directly. By changing the side length of the simulation cell and the frequency of adding new atoms, the deposition rate can be controlled. This approach can pinpoint the competitive processes of thermal diffusion and deposition rate and is the purely computational analysis of the mechanism, without direct relevance to the experiment. Similarly, partial temperature control and free-flying atom deposition setup are used not only for simulation of the growth of a NP but also for flat surface deposition and nanowire growth simulation (see publication **III**).

4.3 Monte Carlo simulations

Monte Carlo method, named after a casino in Monaco, was invented by Stanislaw Ulam and John von Neumann, while they were working on nuclear weapons projects at the Los Alamos National Laboratory [58, 59]. It is a method which relies on repeated random sampling and statistical analysis to compute the results. There is a wide range of simulation techniques based on the Monte Carlo method. In this thesis, we introduce two commonly used methods for atomistic simulations.

4.3.1 Metropolis Monte Carlo

Metropolis Monte Carlo (MMC) was developed in present form by Metropolis, Ulam and Neumann during their study of neutron diffusion [60]. The method is applied for searching the equilibrium state of a system. The algorithm starts from a random configuration of the system. Then a random new state is generated as a follow-up of the current state. The acceptance

probability P of the new state is calculated as such:

$$P = \begin{cases} 1 & \epsilon_1 < \epsilon_0 \\ \exp(-(\epsilon_1 - \epsilon_0)/k_B T) & \epsilon_1 \geq \epsilon_0 \end{cases} \tag{4.12}$$

where ϵ_0 and ϵ_1 are the energies of the current and new states, respectively, T is the temperature of the system and k_B is the Boltzmann constant. Regardless of the starting point, the system will generally converge to the equilibrium state at the end. Although it is also possible that the system may be trapped in some local energy minima for a long time, this problem can be overcome by slow cooling of the system from high temperature, by a so-called *simulated annealing* method [61]. The MMC method is applied for searching the stable structure of NiCr nanoparticles in publication **II**. The MMC method can give reliable results on equilibrium properties, but it cannot be used to study the kinetic evolution of the system. Therefore, kinetic MC method is developed to address the kinetic processes of the studied phenomena.

4.3.2 Atomic Kinetics Monte Carlo

The motivation of the kinetic Monte Carlo (KMC) method is to study the kinetics of slow thermally-activated processes, since MD simulations can only be applied to the processes within 1 μs. Unlike the MMC method where the transition probability depends on the difference of the states ΔE, the transition rate in KMC is based on the transition barrier E_m between the states, as shown in Figure 4.4. The transition rate is calculated by the Arrhenius equation:

$$\Gamma = \nu \exp(\frac{-E_m}{k_B T}) \tag{4.13}$$

where ν is the attempt frequency, which tells how often an attempt is made to exceed the barrier. In atomic simulations, ν is usually assigned to the thermal vibration frequency of atoms, which is about $10^{13} - 10^{14}$ Hz. We can also define the average time τ for a single event to happen $\tau = 1/\Gamma$. To introduce time into the system, the common way is known as the *residence-time* algorithm [62], where the time advances at every MC step by the time interval Δt:

$$\Delta t = -\frac{\log \mu}{\Gamma} \tag{4.14}$$

where μ is a uniform random number in the interval $[0, 1]$, and Γ is the transition rate from Eq. 4.13. It gives a better description of the stochastic nature of the transition processes to include the randomness in time.

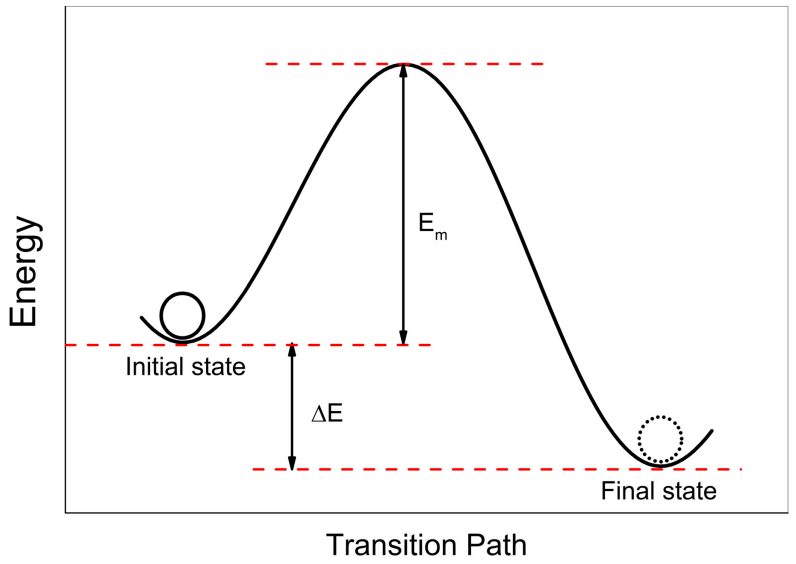

Figure 4.4: Typical transition barrier in KMC

To predict the correct kinetics of the atomic system, it is essential to include all the possible transition processes in simulations. However, the parameterization of a KMC code to describe all processes can make the computational time unmanageable in this case. Approximations have to be made to reduce the total amount of transition paths. For this purpose, in our group the rigid-lattice KMC code, KIMOCS [63], was developed.

In this thesis, we used KIMOCS to simulate the surface evolution of iron surfaces. The result is included in the publication **III**.

4.4 Finite Element Method

The finite element method (FEM) is a numerical technique for obtaining approximate solutions to boundary-value problems of mathematical physics [64]. It was first proposed in the 1940s by Courant to solve problems of equilibrium and vibration [65]. Nowadays, the FEM has been

recognized as a general method widely applicable to engineering and mathematical problems. The fundamental idea is to construct the approximation of the solutions of the partial differential equations (PDEs), based on different types of discretizations and boundary conditions. The simplest approximation of a analytical function is a superposition of linear basis functions:

$$f \approx \mu_h = \sum_i \mu_i \phi_i \tag{4.15}$$

where f is the exact solutions of a PDE, μ_h is the numerical approximation, ϕ_i is the basis functions and μ_i is the coefficients of the functions. Figure 4.5 illustrates this principle for a 1D problem. In this case, there are 10 elements along the portion of the x-axis. We can notice that the uniformly distributed elements, such as $\mu_1\phi_1$, give relatively bad approximation of the original function, therefore, in real application, both the local discrete spacing intervals and the basis functions can be chosen, depending on the problem of interest.

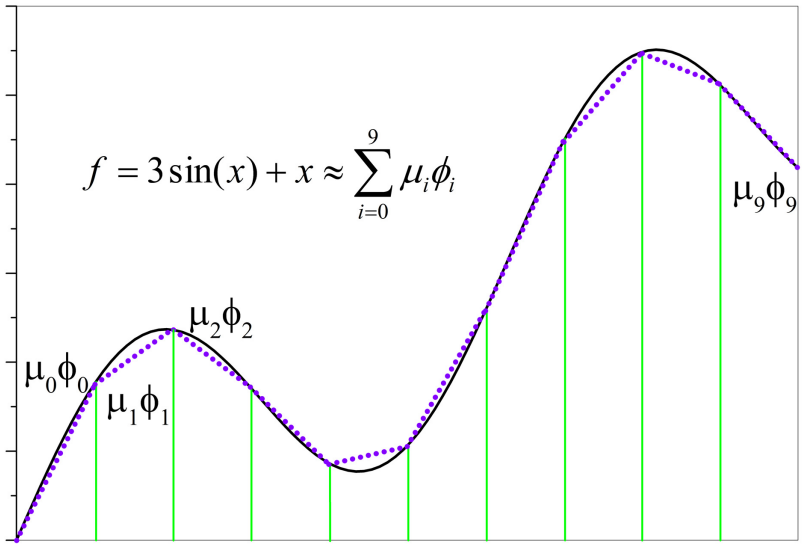

Figure 4.5: The function $f = 3\sin(x) + x$ is approximated with the linear basis functions (dotted purple lines).

In this thesis, we focus on the magnetostatic problem of the magnetron sputtering source. The relevant law of physics is Maxwell's equations. The field intensity H and flux density B must obey:

$$\nabla \times H = J \tag{4.16}$$

$$\nabla \cdot B = 0 \tag{4.17}$$

where J is the electric current density. A constitutive relationship between B and H for each material is:

$$B = \mu H \tag{4.18}$$

where μ is the permeability. If a material is nonlinear, such as pure iron, μ is actually a function of B:

$$\mu = \frac{B}{H(B)} \tag{4.19}$$

If we assume the Coulomb gauge, $\nabla \cdot A = 0$, where A is the magnetic vector potential, by definition, $B = \nabla \times A$, the Eq. 4.16 can be rewritten as:

$$\nabla \times (\frac{1}{\mu(B)} \nabla \times A) = J \tag{4.20}$$

so that magnetostatic problem with a nonlinear B-H relationship can be solved.

In publication **IV**, the configuration modeled by FEM is based on the commercial magnetron source. The calculation was performed by using the FEMM software [66, 67]. The model geometry and the triangle meshes are shown in Figure 4.6.

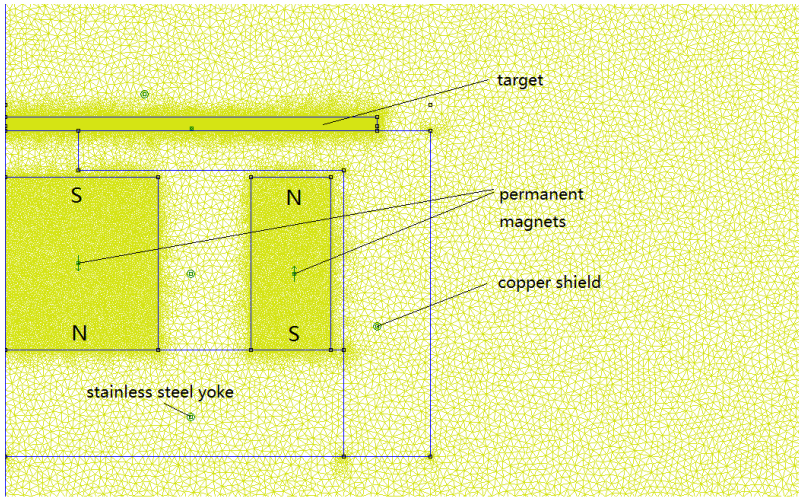

Figure 4.6: Example of the model geometry and mesh.

Chapter 5

Atom-level growth mechanism of nanoparticles

5.1 Formation of crystal Si nanoparticles

In publication **I**, we studied crystallization of silicon NPs in inert gas using the classical MD. The main result from this work is presented here.

Unlike metals condensing through metallic bonds, the semiconductors such as silicon and germanium form solid phase via direction-dependent covalent bonds. This lead to the fact that during the solidification, it is much more difficult to reach the ordered (crystalline) phase for semiconductors than for metals. The cooling rate needed to make high-quality single crystal silicon is from 0.1 K to 100 K per minute [68], which is much lower than the one in the same production process for iron and copper (100 K per minute or above). Recrystallization of bulk silicon was studied by simulation methods to a large extent [69–73], while there is not so many works on NP system.

To elucidate the crystallization process of a molten Si NP, we used MD simulation with inert gas temperature control. The simulation setup followed the approach described in Section 4.2.3. Two well-established Si potentials, the Stillinger-Weber (SW) and Tersoff III (T-III) (see Section 4.2.2) were used for Si-Si interaction. The interaction between Ar atoms was simulated by the Lennard-Jones potential [74]. For Si-Ar interaction, we used the purely repulsive Ziegler-Biersack-Littmark (ZBL) potential [75].

We plot a few exemplary cases in Figure 5.1. The cases are numbered to distinguish the different simulations with the different distributions of initial thermal velocities. Three simulations out of 14 cases showed the crystallization process. Unlike the glass-like phase transition which has a smooth temperature evolution curve, the crystallization of the NPs results in a sharp increase in the temperature evolution curve. We noticed that the simulation cases 3 and 6 are different from the simulation case 11, as the temperature curve of the case 11 increases more abruptly. The angle distribution analysis (fraction of Si atom in disordered environment in Figure 5.1) and topological analysis (number of 6-Ring in Figure 5.1) also indicate that the crystallization of Si NC in the case 11 is closer to a 'complete' one. This difference was confirmed visually by comparing the final structures of the four cases, as shown in Figure 5.2. The case 11 exhibits a single crystal phase, while the case 3 and 6 have polycrystalline structure.

It is worth studying the dependence of the crystallization process on the NP size and the cooling rate, so we simulated also larger Si clusters in the same manner. Similar results were seen in this group of simulation: four simulations out of 11 cases were crystallized with 20 K/ns cooling rate, while none of the 10 simulations showed crystallization with 30 K/ns cooling rate. Here we emphasize the topological analysis of a polycrystalline case. As shown in Figure 5.3, three separate crystallites were identified at the very early stage of the crystallization process. We also notice that the nucleation sites have random shapes rather than spherical ones which is usually the assumption in classical nucleation theory.

Further study was done on the sensitivity of the selected potentials. As discussed in Section 4.2.2, T-III potential has different parameterization from the SW potential, which gives a much higher melting point. Detailed results and figures are shown in publication **I**. We obtained the similar crystallization of a Si NP with 20 K/ns cooling rate. We compared the ratio of the crystallization temperature T_{tr} to the bulk melting point T_m for both potentials, and found that the ratio is about 0.7 and is independent of the potentials.

In this work, we also developed a primary analytical model to fill the gap between the computational simulations and the experiments. The model is used to estimate the temperature evolution of the Si NPs during and after the growth. The model is written as:

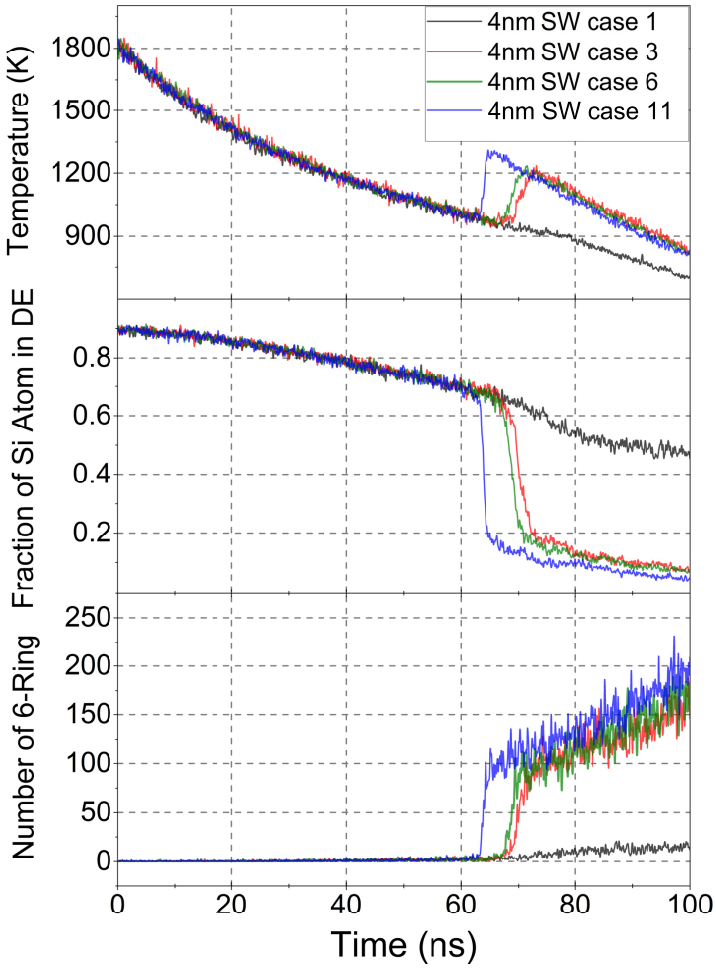

Figure 5.1: (From Publication I) Evolution of the temperature of the silicon NPs (top), the fraction of Si atoms in a disordered environment (DE) (middle), and the number of primitive 6-fold rings (bottom).

$$\begin{cases} \frac{dT(t)}{dt} = \frac{1}{3k_B N(t)}(k\pi r_c^2 v_d \rho_{Ar}(T_{Ar} - T(t)) + 2\pi r_c^2 v_d \rho_{Si} E_{co}) \\ r_c = (\frac{3\overline{V_0}N(t)}{4\pi})^{1/3} \\ N(t) = N_0 + \int_0^t \pi r(t)^2 \rho_{Si} v_d dt = \frac{1}{27}(\pi v_d \rho_{Si} \cdot (\frac{3\overline{V_0}}{4\pi})^{2/3} \cdot t + 3N_0^{1/3})^3 \end{cases} \tag{5.1}$$

where $N(t)$ is the number of the atoms in the NP, r_c is the radius of the NC, k is the energy exchange constant, v_d is the drift velocity of the NP, $\rho_{Ar/Si}$ is the number density of the Ar/Si atoms in the gas phase, T_{Ar} is the temperature of the plasma, E_{co} is the released potential energy

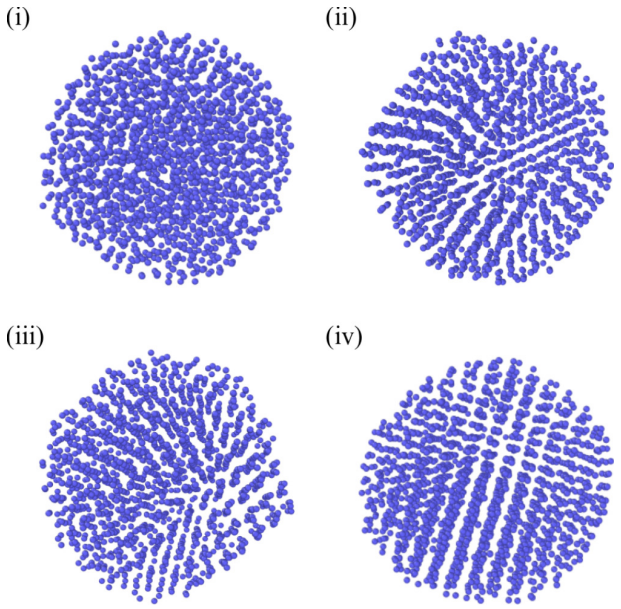

Figure 5.2: (From Publication I) MD snapshots of the final structures of Si NPs: (i) amorphous in case 1; (ii) and (iii) ploycrystalline in cases 3 and 6; (iv) single crystalline in case 11.

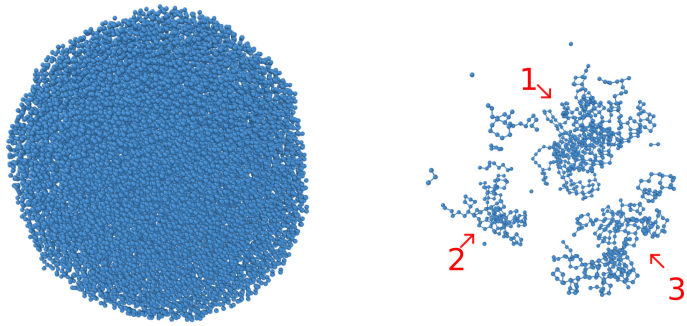

Figure 5.3: (From Publication I) MD snapshot taken from the early point of the crystallization. Topological analysis reveals initial nucleation at the several positions of a 9-nm Si NP.

of the single Si atom coalescence and $\overline{V_0}$ is the average volume for a single Si atom. The model describes a situation that a NP travels through an uniformly distributed Ar/Si plasma region, and the temperature changes as a balance between the cooling by collisions with the Ar atoms and the heating by deposition of the Si atoms. The solution of the model indicates that the favorable conditions for crystallization is as follows: firstly, Si NPs should go through

the hot plasma region to form a hot nanodroplet; secondly, this nanodroplet should be large enough to achieve a relatively low cooling rate. Since a low cooling rate generally promotes crystallization, the large nanodroplet has more chances to crystallize than the small one. The same result can also be seen in the experiments in the publication **I**.

5.2 Surface segregation of NiCr nanoparticle

In publication **II**, we studied surface segregation of NiCr nanoalloy using the classical MD and the MMC method. As discussed in Section 4.2 and 4.3.1, both canonical-ensemble (NVT) MD and MMC simulations can bring atomic system to equilibrium state. The difference between the two methods is that MD simulates the full dynamics of a real physical process while MMC gives only final result, but how exactly a given state of the system was reached, is beyond the concern of MMC method. However, in some practical cases, such as simulation of slow diffusion processes, the time limitation of MD hinders severally the application of this method. On the other hand, MMC methods allow one to sample the ground state more efficiently, avoiding costly calculations of dynamic interaction of all atoms. In this work, MD results were used as a physical present of the surface segregation, while MMC results can be regarded as the very end of the MD simulations.

As shown in Figure 5.4 (f, g, h), the experimental results indicates that upon annealing, the $Ni_{0.95}Cr_{0.05}$ NP transforms into a structure of a Ni-rich core and a Cr-O shell. The driving force behind can be both oxidation or surface-energy minimization. In this thesis, we tried to understand which of two physical processes drives the surface segregation of Cr in NiCr NPs. Common knowledge is that Cr is usually used in stainless steels to form a dense surface chromium oxide layer to prevent further oxidation in bulk. This explanation, in principle, could also be applied to a NP system. However, it was shown experimentally that surface segregation was observed in oxygen-free environment [23, 76–79]. It is a nontrivial effort to see whether surface segregation can occur in NiCr NPs.

To elucidate the segregation mechanism, we simulated the evolution of a 3-nm $Ni_{0.95}Cr_{0.05}$ NP at 600 K for 200 ns. The interatomic potential utilized for this purpose was the EAM potential recently developed by Bonny et al. [46]. Cr segregation is investigated through the evolution of the average short-range order (SRO) parameter, as defined by Cowley [80]:

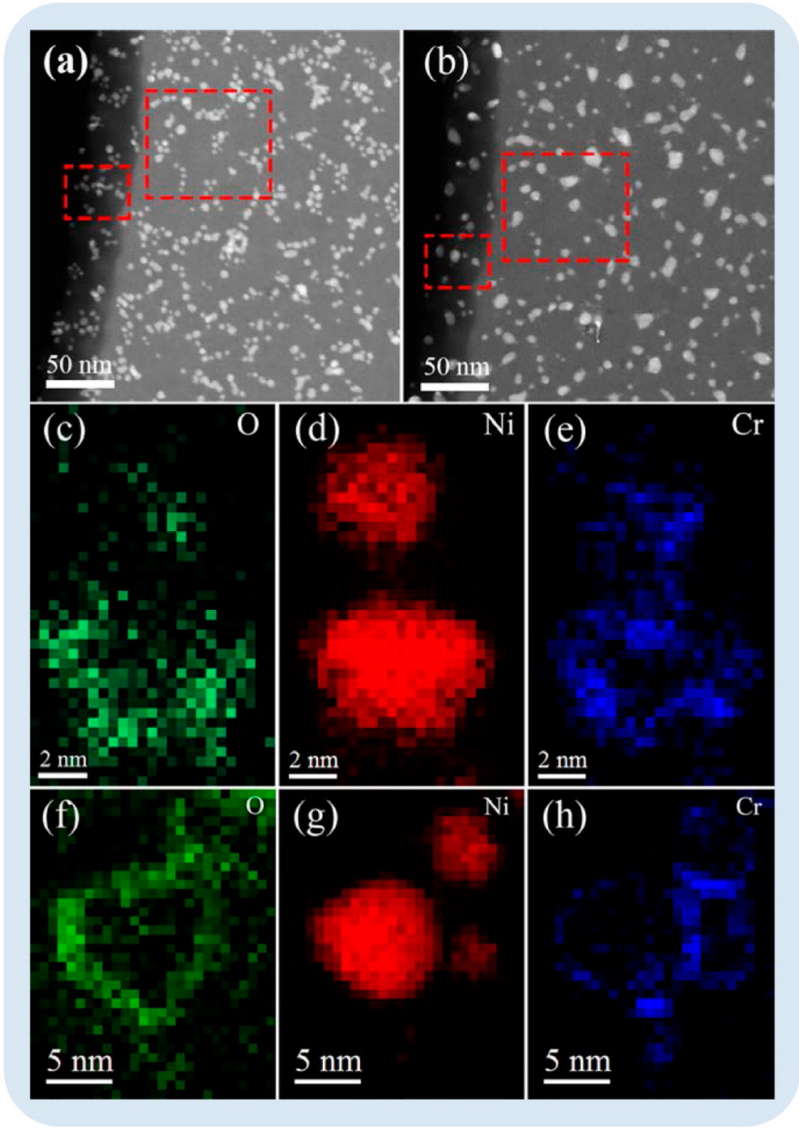

Figure 5.4: (From Publication II) STEM images of NiCr alloy NPs taken before (a) and after (b) annealing. Electron energy loss spectroscopy (EELS) elemental maps for O K edge, Ni $L_{3,2}$ edge and Cr $L_{3,2}$ edge of representative NPs taken before (c-e) and after (f-h) annealing at 823 K in vacuum show that the as-grown NPs have a Ni-rich core with a Ni-Cr-O shell and the annealed ones have a Ni core and a Cr-O shell.

$$\alpha_i = 1 - \frac{p_{xyz}}{\chi} \tag{5.2}$$

where p_{xyz} is the probability that an atomic site with coordinates x, y and z, is occupied by

an atom of the other species, and χ is the overall proportion of this atomic specie. The SRO parameter is a value within the interval [0, 1]. It is obvious that when the system is randomly distributed, a zero value of the average SRO parameter is expected.

As shown in Figure 5.5, the final structure of the 3-nm $Ni_{0.95}Cr_{0.05}$ NP is a truncated tetrahedron with the FCC lattice. We found that Cr atoms preferentially gather on vertex and edge sites. Although Cr lattice is BCC by nature, such small islands of segregated Cr, which are embedded in the FCC Ni matrix, cannot rearrange themselves into BCC lattice. We also calculated the surface energy for species in FCC lattice and found that Cr low-index FCC surfaces would be energetically expensive. This leads to the fact that it is more stable for Cr atoms to stay at less close-packed facets.

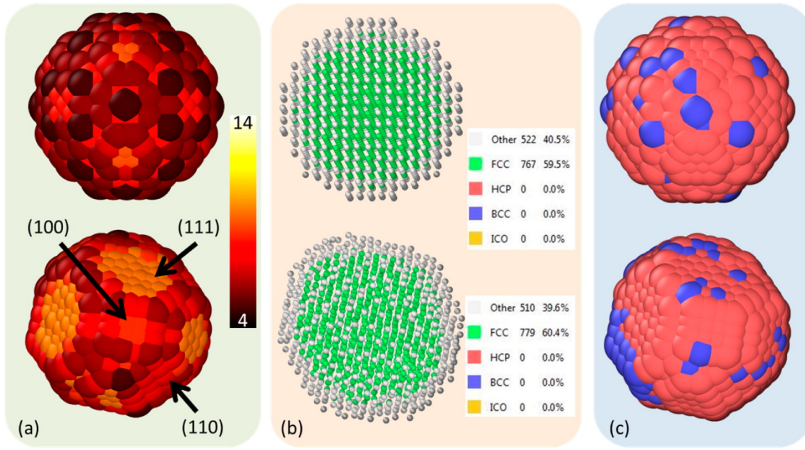

Figure 5.5: (From Publication II) Initial and final structures of a 3-nm $Ni_{0.95}Cr_{0.05}$ NP. After annealed at 600 K, the NP transfers into a truncated octahedron with low-index facets. Some Cr atoms (blue atoms in (c)) segregate on the surface.

We also noticed that Cr atoms migrate very slowly at 600 K, so there is not clear tendency of surface segregation. To overcome the limitation, we set the annealing temperature to 1200 K. As shown in Figure 5.6, the average SRO parameter and the total potential energy were monitored during the 200 ns annealing. A clear tendency of Cr segregation is seen. However, full segregation was not reached even at 1200 K simulation.

We further utilize MMC to search the ground state of the 7-nm $Ni_{0.95}Cr_{0.05}$ NP. The simulation is set to calculate the potential enrgy of the NP at each MC step and switch the type of two

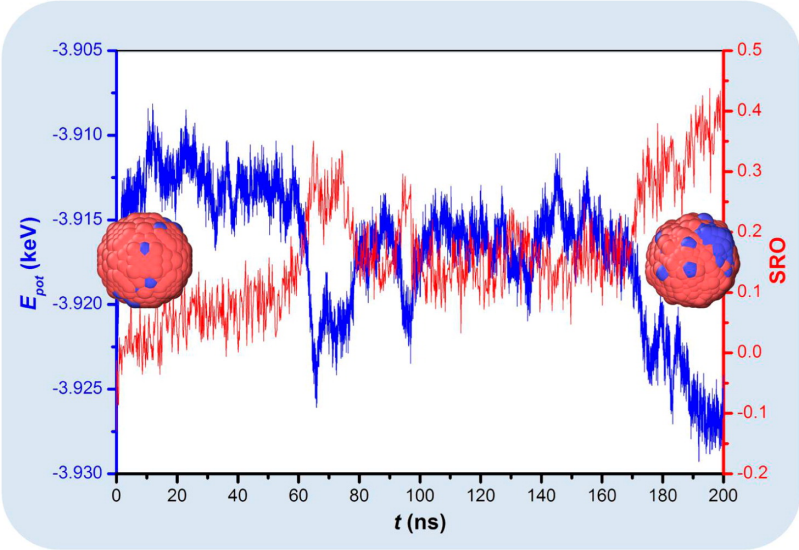

Figure 5.6: (From Publication II) Evolution of the average SRO parameter (red curve) and the total potential energy (blue curve) of a 3-nm $Ni_{0.95}Cr_{0.05}$ NP at 1200 K

Ni and Cr atoms every 20 step. As shown in Figure 5.7(b), the initial state with randomly distributed Cr atoms has relatively high potential energy. The final state (Figure 5.7 (d)) with the converged potential energy has a fully segregated Cr phase. One detail of the simulation is that Cr atoms were first exchanged to the surface and formed a core-shell like structure (Figure 5.7(c)). This intermediate state is very similar with the annealed structure in the experiments and MD simulations. The reduction of the potential energy is also very abrupt during this process. A test simulation showed that the potential energy drops 0.3 to 0.5 eV for a single Cr atoms moving from bulk to surface.

Further analysis on the atomic potential energy and stress are shown in Figure 5.8. The segregated FCC Cr phase has higher potential energy comparing to the Ni phase, but it is much lower than the initially isolated Cr atoms. The reduction of the potential energy is corresponding to the atomic stress relaxation. Cr atoms in BCC lattice have larger first- and second-nearest neighbour distance than they are in FCC lattice. The optimal numbers of bonds for BCC Cr is 8 and 6 with the first and second nearest neighbours, so it is very energetically unfavorable for Cr atoms to stay in FCC lattice. We have seen in a test simulation that Cr phase transitions into BCC lattice with much higher Cr concentration in NiCr NPs.

After the Cr atoms switch to the surface, several separated Cr 'islands' immediately formed.

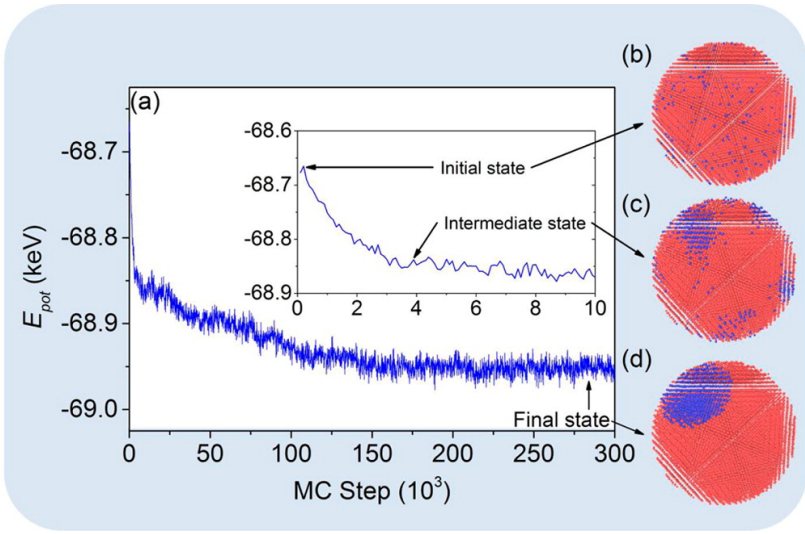

Figure 5.7: (From Publication II) (a) Evolution of potential energy of a 7-nm $Ni_{0.95}Cr_{0.05}$ NP at 600 K. (b) Initial state of the NP with Cr atoms in blue and Ni atoms in red. (c) Intermediate state of the NP at 4000 MC step. (d) Final state of the NP.

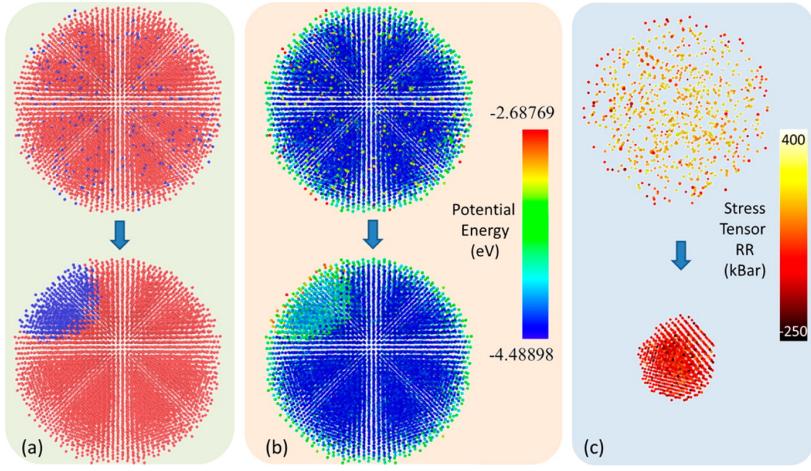

Figure 5.8: (From Publication II) (a) $Ni_{0.95}Cr_{0.05}$ NP before and after phase segregation. (b) Color coding of potential energy: the potential energies of Cr atoms reduce upon Cr segregation. (c) Color coding of atomic stress tensor RR: Cr segregation also led to a substantial reduction of atomic stress.

However, it takes 25 times more iterations, at least, for these islands to combine into one. In the real kinetic process where no simple swapping of atoms takes place, this will be even more difficult, since the mobility of the Cr island is very slow. In most cases, Ni-core-Cr-shell structure will be the main outcomes obtained in experiments.

5.3 Formation mechanism of Fe nanocube

From the two sections above (Section 5.1 and 5.2), we see that upon cooling and annealing, NPs will drive themselves to the lowest energy state. The time scale depending on process and temperature, can span from microseconds to days. The outcome does not have any trace of the condensation history. In publication **III**, we show that the shape control of iron NP can be achieved by controlling the condensation process in solid state.

Non-spherical NPs have been synthesized and studied in various environment [81–87]. As discussed in Section 3.1, the surface minimization will lead to a spherical or roughly spherical polyhedral shapes of NP. For BCC iron (Fe), this argument is valid as well. As shown in Figure 5.9, molecular statics results of five NP shapes with different sizes reveals that the rhombic or truncated rhombic dodecahedron (RD and TRD in Figure 5.9, respectively) are the most stable shapes of Fe NP. For BCC iron, the closest packed {110} facet has the lowest surface energy [88, 89]. {100} facet has higher surface energy, but can truncate the NP into more spherical shape. However, the cubic shape with six {100} surfaces are consistently the least stable structure of all sizes.

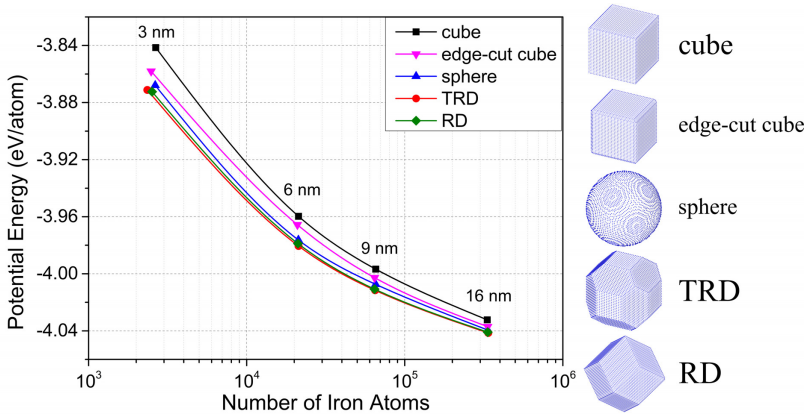

Figure 5.9: (From Publication III) Average potential energy per atom of Fe NP as a function of NP size. Five shapes shown on the right hand side are considered. The truncated rhombic dodecahedron (TRD) is the most stable shape in the investigated range of NP size.

Further simulation on liquid-solid phase transition verified the stability of RD or TRD shapes. As shown in Figure 5.10, by assuming a liquid NP during the early growth stage, we simulated

the cooling process of a 13 nm Fe NP in an inert gas atmosphere. The approach is almost the same as what is used in publication **I**. During the first 45 ns, the Fe NP cools from 1800 K down to the phase transition temperature at about 1000 K. At this point, an abrupt first-order phase transition occurs and the Fe NP crystallize to BCC lattice. Upon further cooling, the final structure of the NP is a TRD shape with 6 $\{100\}$ and 12 $\{110\}$ planes.

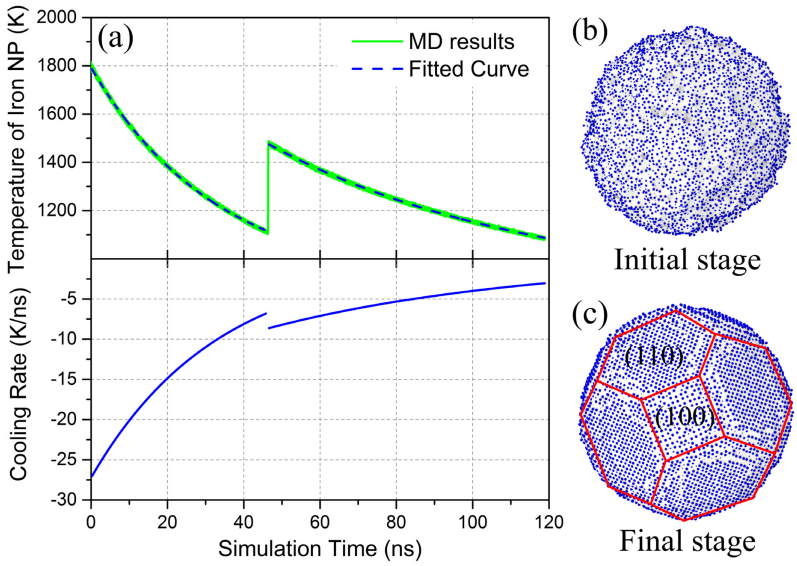

Figure 5.10: (From Publication III) (a) Evolution of temperature (top) and cooling rate (bottom) of an Fe 13 nm Fe NP. (b) The initial stage of the NP is in liquid phase. (c) After cooling down to 1100 K, the NP solidified into a BCC lattice of TRD shape.

However, the experimental results from the magnetron sputtering source shows that at certain gas flow rate and dc power, the outcome of the Fe NPs can change from spherical shape to cubic shape. It is clear that this observation can not be explained by the energy minimization, so we further look at the kinetic effect from the deposition process.

By using the MD approach described in Section 4.2.3 and the KMC model *KIMOCS*, we simulated the solid-state growth of spherical Fe NPs. As shown in Figure 5.11, two temperatures below the phase transition point were tested. Both MD and KMC methods give very similar results. In the 1000 K (high T) case, the Fe NP grows into a TRD shape because of the intensive surface diffusion, while in the 500 K (low T) case, the final structure of the NP has a large

fraction of {100} facets. Closer observation at the very early stage of growth indicates that at low temperatures, the small nano-islands cumulatively grow in {110} direction and close up the {110} facets eventually. This leads to the fact that the growth modes of {100} and {110} facets may be essential to the final shape of the Fe NP.

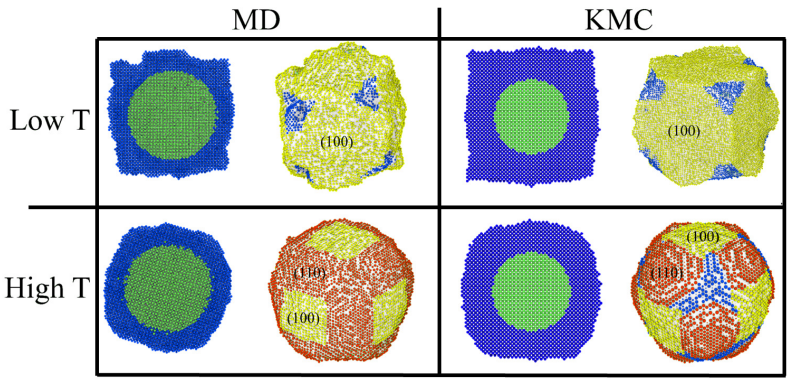

Figure 5.11: (From Publication III) Cross sections (left) and 3D images (right) of the final Fe NPs obtained in MD and KMC simulations of deposition process at 500 K (low T) and 1000 K (high T). The different colors of the surface atoms represent the {100} (yellow), {110} (red) and other faceted surface (blue).

To investigate the growth modes specific to the {100} and {100} surfaces at different temperature, we narrowed down the problem into a two-dimensional nanowire (NW). In these simulations, we used two different deposition rates, which are labelled as high and low R_d in Figure 5.12. The constant temperature control was only applied to the core atoms of the NW as described in Section 4.2.3, while the temperature of the surface and deposited atoms was allowed to evolve freely. Three initial temperatures, 500 K, 700 K and 1200 K, were chosen. As shown in Figure 5.12, six final cases can be regrouped into three pairs by the final shapes of NWs: square, truncated square and round shapes. It can be seen that at three temperatures and two deposition rates, the growth model of the {100} facets is layer-by-layer growth mode, while the {110} facets grow via the island growth mode at low temperature, and generally switch to layer-by-layer growth at elevated temperature. Here, we also emphasize the effect of the deposition rates. At 1200 K, the final structures of NWs with high and low R_d are truncated square and round shape, respectively. This fact indicates that the growth mode of {110} faces is not only dependent on the temperature, but also the deposition rate.

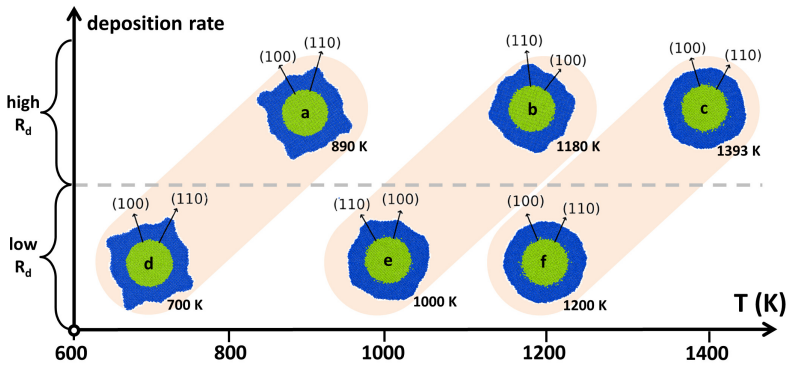

Figure 5.12: (From Publication III) Final shapes of Fe nanowire cross sections obtained by MD simulations of deposition process with different deposition rates, R_d. High and low R_d correspond to introducing at random a newly arriving surface atom every 100 and 1000 MD steps.

The self-diffusion barriers of Fe adatom on $\{100\}$ and $\{110\}$ facets reveal the atomic mechanism of the different surface growth modes. As illustrated in Figure 5.13, atoms landing on $\{110\}$ surfaces diffuse rapidly, and almost immediately form single-layer nano-islands, even at low temperatures, due to low migration ($\sim$ 0.27 eV) and relatively high detachment barriers ($\sim$ 0.58 to 1.0 eV). The newly deposited atoms, which land on top of the already existing nano-islands, diffuse only within the latter, barely having an opportunity to climb down (in this case, the Ehrlich-Schwoebel barrier is between 0.64 and 0.72 eV, depending on specific diffusion pathway). At 500 K, the average time for the rapid diffusion of the Fe adatom on $\{110\}$ facet to happen is about 52.7 ps ($\tau = 1/\nu \exp(-E_m/k_B T)$ with $\nu = 10^{13}$ Hz) and the one for climbing down is 1.81 μs. The difference in the residence time needed for both transitions to happen shows that the former is a way more frequent than the latter. This fact explains why these islands are stable and grow in all dimensions until they finally take over the entire $\{110\}$ surface in accord with a Volmer-Weber-like (VW, island growth in Figure 5.13) mechanism. On the other hand, growth on the $\{100\}$ surfaces (as seen in the same NWs of Figure 5.12) appears to be rather flat. However, closer inspection shows limited nanoscale roughness on the $\{100\}$ facets as well. This is explained by the high atomic migration ($E_m \geq 0.72$ eV) and Ehrlich-Schwoebel barriers (1.04 eV) that allow nano-islands to grow initially upwards. However, since the sides of the growing nano-islands have preferentially $\{110\}$ facets, after the formation of about three layers only, the fast diffusion specific to $\{110\}$ surfaces comes into play, as shown in the top-middle atomic-scale schematic of Fig. 5.13. This prevents further

upward growth of the nano-island and leads to its flattening; thus the overall growth is dictated by a Frank-van-der-Merwe-like (FM, layer-by-layer growth in Figure 5.13) mechanism. The difference of barriers become insignificant at high temperature (1000 K or higher), however the growth mode of the two facets are a trade-off between the atomic diffusion and deposition. For example, at 1000 K, the average time for a single event with 1 eV barrier to happen is about 10 ns, however, if the deposition process is finished within this time span (as the case in MD simulations), it will still lead to Volmer-Weber-like growth on the {110} facets.

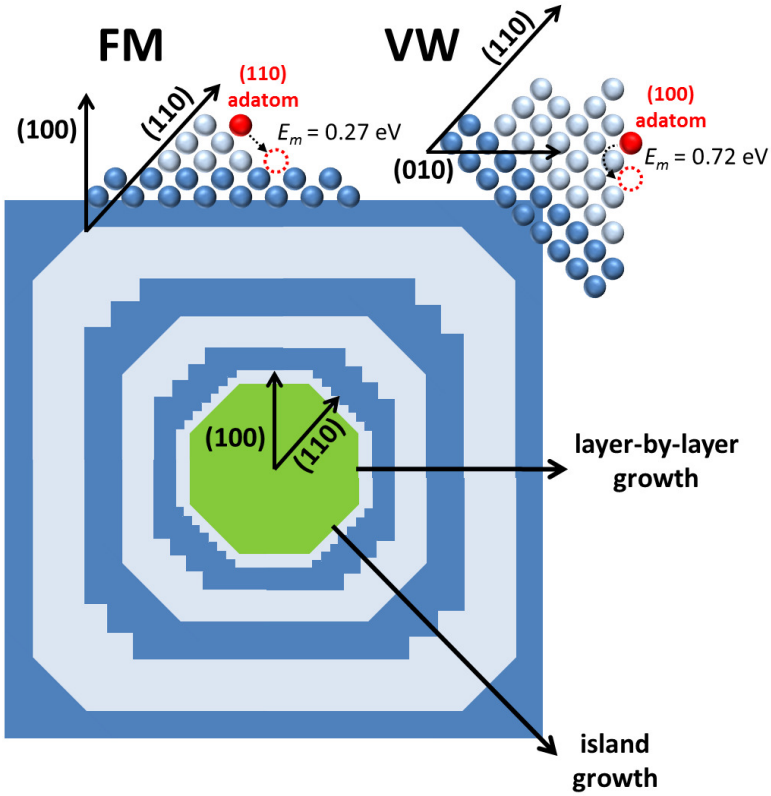

Figure 5.13: (From Publication III) Schematic illustration of an initially faceted TRD NP growing into a cubic shape via competing atomic deposition and surface diffusion mechanisms. The alternating light and dark blue colors of the newly-deposited adatom layers imply temporal evolution. Nanoislands of {110} and {100} sides are grown on {100} and {110} facets, respectively, as shown in the zoomed in areas. Different growth modes – {110} facets grow via a Volmer-Weber-like mechanism and {100} facets via a Frank-van-der-Merwe-like mechanism – lead to the different effective growth rates.

We also performed the same simulation with the KMC model. To directly compare with the experimental result, we mapped all the combinations of deposition rates and temperatures. The pin-pointed map which we named a 'shape diagram' is presented in Figure 5.14. The purple, blue and red points are the KMC samples, and the yellow points are corresponding to the MD results shown in Figure 5.12. There is a clear transition zone (blue points) between the cube region (red points) and the spherical/TRD region (purple points). We give a quantitative analysis of the diagram, which, in the next section, will enable the construction of a full analytical model that can be useful as a reference guide for future NP growth experiments.

The average residence time Δt_r before a diffusional jump of a surface atom occurs at a given temperature, T, can be defined as the inverse of the diffusion transition rate given by the Boltzmann equation [90]:

$$\Delta t_r = (\gamma_0 exp(-\langle E_m \rangle / k_B T))^{-1} \tag{5.3}$$

Here γ_0 is a prefactor which includes the number of available transitions and the attempt frequency of a jumping atom, and k_B and $\langle E_m \rangle$ are the Boltzmann constant and the effective migration barrier for an average diffusional jump of a surface atom, respectively. On the other hand, we can estimate the time, Δt_d, needed to cover the entire surface via the deposition.

$$\Delta t_d = \frac{N_a}{R_d A_{hkl}} \tag{5.4}$$

Here, R_d is the deposition rate, whereas A_{hkl} is the area per unit cell with the corresponding Miller indices (hkl) for the (100) or (110) surfaces. N_a is the number of atoms, which is unity if growth of a single atomic layer is considered.

If this time, Δt_d, is shorter than the residence time between diffusion transitions, diffusion is restricted, and both surfaces grow uniformly, inducing no change to the initial shape, which remains spherical. By equalizing these two time periods, we can designate points in the Fe NP shape diagram (see Figure 5.14) that correspond to final shapes that are in-between of cubic and spherical ones, as obtained by our MD and KMC simulations. The curve going through these points constitutes a border separating the areas of clearly cubic and clearly spherical final shapes of the Fe NPs.

$$R_d = \frac{N_a \cdot \gamma_0 exp(-\langle E_m \rangle / k_B T)}{A_{hkl}} \tag{5.5}$$

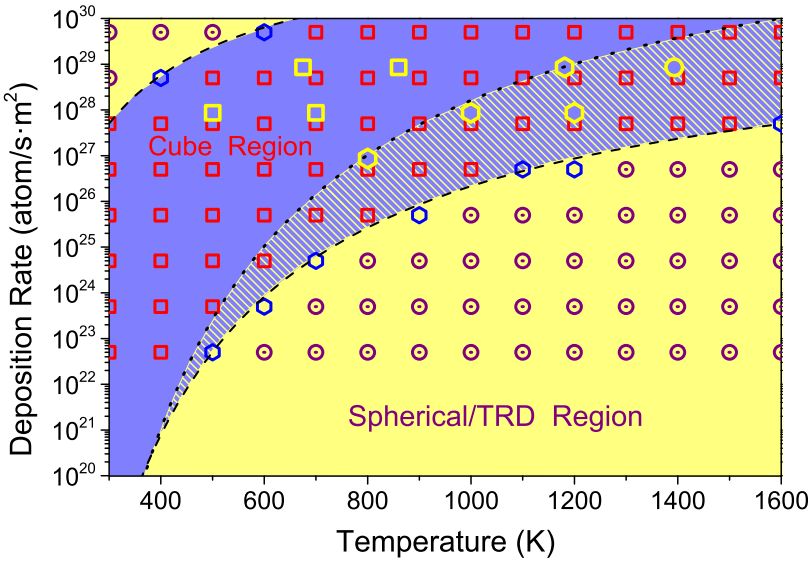

Figure 5.14: (From Publication III) Comprehensive deposition rate–temperature diagram of final Fe NP shapes. Results were obtained by simulating Fe NWs by KMC. Square and circular markers indicate cubic and spherical shapes, respectively. The yellow markers are MD results. The hexagonal shaped markers stand for irregular shapes which fall in between cubic and spherical shapes. The dashed and dotted curves are the exponential fits to the KMC and MD results, respectively. The hatched area between two exponential fits indicates the uncertainty of the present simulations due to the use of different methods. However, the two simulation methods converge at low deposition rates relevant to the experiment.

By substituting all pre-factors before the exponent with a single fitting parameter $\gamma = N_a \cdot \gamma_0 / A_{hkl}$, we can fit the two transition lines for KMC and MD data points, respectively. We note that the curves fitted to the MD and KMC results are described by similar, but not identical, fitting parameters. The most intriguing difference is in the $\langle E_m \rangle$ value, which is higher for the MD results and amounts to 0.94 ± 0.11 eV compared to 0.72 ± 0.04 eV for KMC. This divergence stems from the contribution of diffusion barriers that cannot be predicted by KMC. For instance, collective many-body or concerted jumps become possible on a $\{100\}$ surface at high temperatures. These barriers were estimated as $\langle E_m \rangle \sim$ 1.0 to 1.22 eV and only allow jumps very rarely at low temperatures. However, the MD and KMC results nicely converge at

low temperatures and low deposition rates; it is also worth noting that this is the regime relevant to the experimental conditions of the magnetron sputtering inert gas condensation method.

With a further developed analytical model from the Eq. 5.1 discussed in Section 5.1, we try to fit the experimental data into the shape diagram. The new model considers a NP as a static sphere in the gas phase. Ar and Fe atoms collide with the NP with thermal velocities. A black-body radiation term is added to the $dT(t)/dt$ equation to correct the long-term evolution of temperature. The number density of Fe atoms is not a constant, but a decay function as $\rho_{Fe}(t) = \rho_{Fe}(0) - N(t)/V$. The new equation group is written as:

$$\begin{cases} \frac{dN(t)}{dt} = \pi \cdot r_c^2 \cdot (\rho_{Fe} - \frac{N(t)}{V}) \cdot v_{Fe} \\ \\ \frac{dT(t)}{dt} = \frac{\pi r_c^2}{3k_B N(t)} \cdot [3k_B \rho_{Ar} v_{Ar}(T_{Ar} - T(t)) + 2(\rho_{Fe} - \frac{N(t)}{V}) \cdot v_{Fe} E_{co}] \\ -8\pi r_c^2 \sigma \epsilon (T(t)^4 - T_{Ar}^4)/(3k_B N(t)) \end{cases} \tag{5.6}$$

From the analytic model, the evolution of the deposition rate can be derived from the growth rate of the NP, $dN(t)/dt$, divided by the surface area of the NP, $A_c(t) = 4\pi r_c^2(t)$. Then, from the first equation of the system of equations (5.6), we obtain:

$$R_d = \frac{dN(t)/dt}{A_c(t)} = \frac{1}{4}(\rho_{Fe} - N(t)/V) \cdot v_{Fe} \tag{5.7}$$

If we plot the evolution of the temperature of NP, the solution of the Eq. 5.6, as a function of the deposition rate, the solution of the Eq. 5.7, together with the shape diagram in Figure 5.14, the result is as shown is Figure 5.15. With certain experimental condition, although the starting point of the NP growth is always in Spherical/TRD region, the final shape of the NP depends on the ending point in the shape diagram. It is clear that with the highest power, fast deposition in the early stage will lead to fast cooling during the last or late stage. In the very last stage of the NP growth, the mechanism described in Figure 5.13 becomes dominant and drives the NP into a cubic shape.

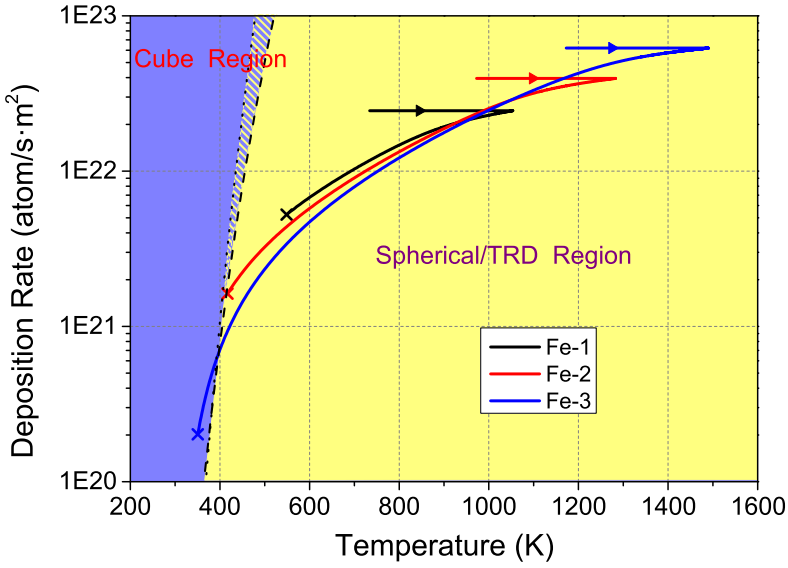

Figure 5.15: (From Publication III) A joint plot of the shape diagram and the analytical model. At the beginning of the condensation process the clusters are formed in a high-density region, leading to their rapid heating at the same deposition rate (horizontal top part of the three curves). Beyond the hot plasma region, the deposition rate decreases and the clusters cool down due to collisions with the carrier gas and black-body radiation. The decrease of deposition rates and temperatures ends (cross markers) at the exit of the Fe NPs from the condensation chamber.

5.4 Bimodal distribution of Fe nanocube

In publication **III**, we demonstrate how the macroscopic conditions of the magnetron sputtering source can determine the microscopic shape of Fe NPs. In publication **IV**, we show that the size distribution of Fe NPs can be controlled by the magnetic property of the sputtering target. A unique bimodal size distribution can be achieved by just changing the thickness of the ferromagnetic iron target.

As shown in Figure 5.16 (a), the magnetron sputtering source has three main components which are the permanent magnets, the copper shield and the target. The magnetic field generated by the permanent magnets works as a trap for secondary electrons, thus the Ar ionization is enhanced in the confined region. The ionized Ar atom will be accelerated alone the electric field which is normal to the target surface, therefore, the most etched part of the target is directly under the most enhanced ionization region where $B_z = 0$. When magnetic targets (Fe, Ni,

Co, etc.) are used, they can affect the magnetic field configuration via a screening effect. This effect, arising from the high permeability of ferromagnetic materials, induces magnetic flux through the target, allowing only a small part to leak out and sustain the magnetron plasma. As shown in Figure 5.16 (c), we performed the FEM calculations to analyze the effect of screening of magnetic field by ferromagnetic targets. For reference, we compared the magnetic flux densities for the cases of the ferromagnetic Fe targets with a paramagnetic Ti target (Figure. 5.16 (c), top). Primarily, the magnetic field strength near the target surface, which dictates the plasma density, shows a gradual decrease with target thickness, especially for the 1.0mm Fe target (Figure. 5.16 (c), bottom). Moreover, the magnetic field distribution is also drastically modified in the 1.0mm case due to the screening effect induced by the Fe target.

The most enhanced ionization regions are labeled with red circles in Figure 5.16 (c). It is associated with the zero point of the normal magnetic field density, in Figure 5.16 (d). In a 1mm iron target case, the normal field density is much less than the one in Ti target. This further leads to the erosion region becoming wider and distorted, as shown in Figure 5.16 (e). A closer examination of the etching profile of the 1 mm iron target reveals that there are two different etched zones with different slopes. As shown in Figure 5.17, two corresponding incident angle of Ar ion sputtering θ_1 and θ_2 are about 45 and 70 degree, respectively. It is known that the sputtering yield is dependent on the incidence angle [91, 92]. An analytical model was fitted in 1983, assuming the amorphous surface of the target [92, 93]. Here, we used MD to study this effect. The result in Figure 5.17 (c) are the statistical sputtering yields by averaging 100 simulations for each data point. The Ar ion was initially placed 10 Å above the Fe surface with three different low-index facets: $\{110\}$, $\{100\}$ and $\{111\}$. The energy of the Ar ion is set to 300 eV and incidence angles are chosen as 0, 15, 30, 45, 60, 75 degree. The maximum sputtering yield $Y_{Fe}^{Ar} = 2.5$ is at about 45 degree for all three facets, while it is only 0.6 at 75 degree. This difference induces a major modification of the Fe : Ar atomic ratio in two clearly separated nucleation and growth zones. If we apply the analytical model described in Eq. 5.6 to investigate the plasma density dependence on the NP growth, a 5-fold difference of Fe atom densities (ρ_{Fe1} and ρ_{Fe2}, estimated from the sputter yields mentioned above) results in a 50-fold increase in the number of Fe atoms in a single NP.

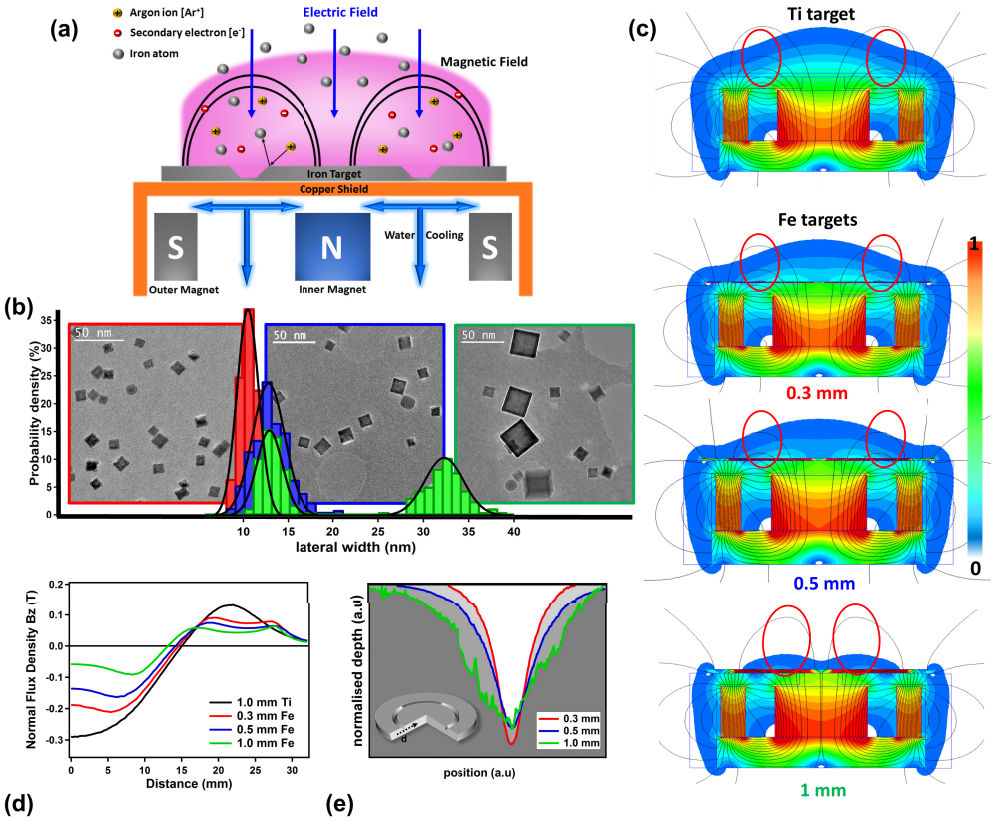

Figure 5.16: (From Publication IV) (a) Schematic illustration of the setup of the megnetron sputtering source. (b) the size distribution of the Fe nanocube from 0.3 , 0.5 and 1.0 mm thickness target (from left to right). (c) FEM simulations of the magnetic field distribution for the setup in (a). The color coding is the normalized field density. (d) The normal field density B_z 1.9 mm above the copper shield. (e) The surface profile of the erosion region on the iron target in three thickness.

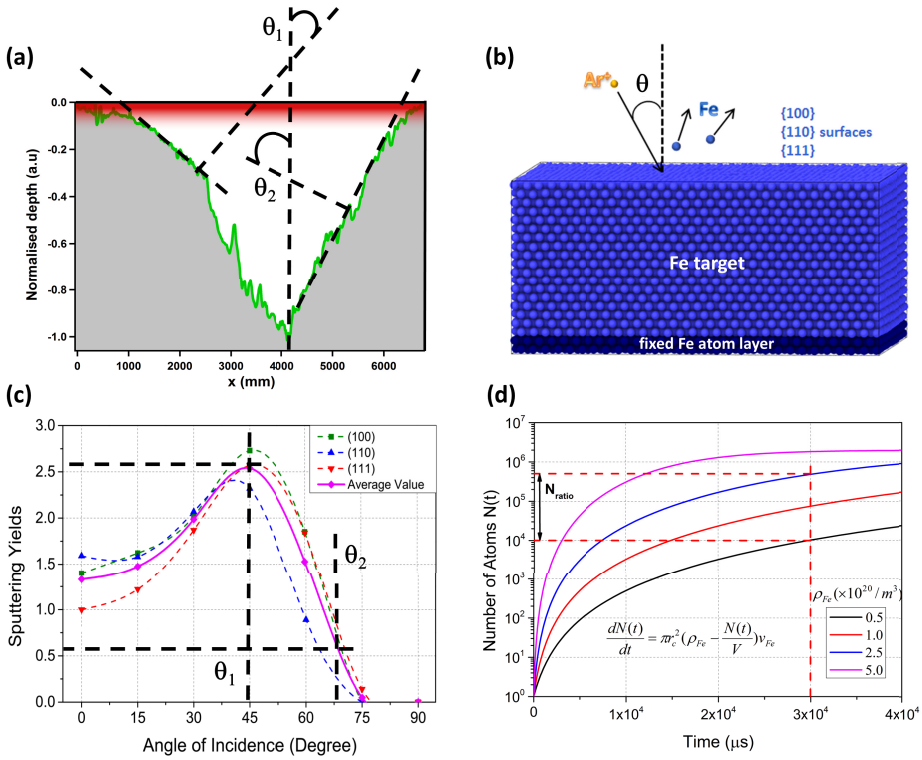

Figure 5.17: (From Publication IV) (a) The etching profile measurement after Fe nanocube deposition with the corresponding incidence angles, namely θ_1 and θ_2 for the 1 mm target thickness case. (b) The initial setup of the sputtering yield MD simulations. Incident Ar ions (yellow) sputter Fe atoms (blue) from surfaces with different crystallographic orientation ({100}, {110} and {111}). Dark blue atoms are fixed. Periodic boundary conditions is applied to the sides of the simulation cell. (c) Angular dependence of the sputtering yield using MD simulations for three different Fe {100}, {110} and {111} surfaces at 300eV ion energy. (d) Analytical estimation of the number of Fe atoms in NP as a function of time.

Chapter 6

Conclusions

In this work, we studied the atomic level growth mechanism of NPs in magnetron sputtering inert gas condensation. Three exemplary systems were studied in this thesis. Firstly, we showed that the crystallization of Si NPs is a general process that can be expected to occur in the inert gas condensation method. The crystallization temperature of the Si NP is dependent on the size of the system, whereas the probability of crystallization is dependent on the initial temperature of the formed cluster and the cooling rate. Secondly, Cr surface segregation in $Ni_{0.95}Cr_{0.05}$ NP was studied by the classical MD and MMC. The result shows that a Ni-core-Cr-satellites configuration, upon condensation and annealing, is low-energy state due to surface energy and stress minimization. Thirdly, we demonstrated that the formation of Fe nanocubes in magnetron sputtering condensation can be explained by the different diffusion behaviors of atoms deposited on $\{100\}$ and $\{110\}$ surfaces at different temperatures. We also introduced the magnetic target thickness as a crucial parameter in the size distribution of Fe NPs, and revealed the influence of magnetic screening effect on Fe nanocube formation.

The results shows that the growth process of NPs depends sensitively on the experimental conditions, such as dc power, inert gas flow rate, cooling system, aggregation length and materials of the target. To include all these parameters into computational simulations, multi-scaled simulation methods need to be used. We established an efficient approach of simulations to study the different stages of NP growth, beginning from the sputtering process to the solid-state growth process. The methods used in this thesis include the classical molecular dynamics, Metropolis Monte Carlo, kinetic Monte Carlo, finite element model and analytical model. By combining these simulation techniques, we were able to examine the NP process in a wide

range of time and spatial scale with atomic resolution. In return, the computational simulations works as a step forward to the precise control of NP properties in experiments.

Acknowledgements

I wish to thank the former head of the Department of Physics at the University of Helsinki, Prof. Juhani Keinonen, and the current head, Prof. Hannu Koskinen, as well as the head of the Accelerator Laboratory, Prof. Jyrki Räisänen, for providing the facilities for the research presented in this thesis.

I want to express my gratitude and respect to my supervisors Dr. Flyura Djubrabekova and Prof. Kai Nordlund, as the ancient Chinese saying, "*Teachers for one day should be respected for a lifetime.*" Thank You for setting yourselves examples as real scientists. Thank you for your ceaselessly guidance, support and trust. Thank you for your not only scientific expertise but also delightful personality.

This work is in large part the result of a rewarding collaboration with the Nanoparticles by Design Unit at Okinawa Institute of Science and Technology (OIST). I thank Prof. Muhkles Sowwan for his unlimited inspiration and financial support to my research trip to OIST. I acknowledge my collaborators Dr. Panagiotis Grammatikopoulos, Dr. Jerome Vernieres, Dr. Vidyadhar Singh, Dr. Cathal Cassidy and Dr. Stephan Steinhauer. Special thanks to Dr. Panagiotis Grammatikopoulos for the help during the trips to OIST.

It is a great pleasure to share the working environment with my brilliant colleagues. I would like to express my appreciation to Antti, Morten, Ekaterina, Elnaz, Wei, Henrique, Ville, Laura, Fredric, Annika, Andrey, Alvaro and also several former colleagues, Harriet, Stefan, Mohammad, Aleksi and Konstantin. Thank you all for your kindly help on my scientific problems and friendly interaction in my daily life!

Financial support from The doctoral programme in Materials Research and Nanosciences (MATRENA) is gratefully acknowledged.

Finally, I wish to thank my parents and my wife for all the love and trust.

Helsinki, August 18th, 2016

Junlei Zhao

Bibliography

[1] C. P. Poole Jr and F. J. Owens. *Introduction to nanotechnology*. John Wiley & Sons, 2003.

[2] B. Jamtveit and P. Meakin. *Growth, dissolution and pattern formation in geosystems*. Springer, 1999.

[3] F. Dumestre, B. Chaudret, C. Amiens, P. Renaud, and P. Fejes. Superlattices of iron nanocubes synthesized from fe[n(sime$_3$)$_2$]$_2$. *Science*, 303(5659):821–823, 2004.

[4] M. Azubel, J. Koivisto, S. Malola, D. Bushnell, G. L. Hura, A. L. Koh, H. Tsunoyama, T. Tsukuda, M. Pettersson, H. Häkkinen, et al. Electron microscopy of gold nanoparticles at atomic resolution. *Science*, 345(6199):909–912, 2014.

[5] X. Qi, T. Balankura, Y. Zhou, and K. A. Fichthorn. How structure-directing agents control nanocrystal shape: Polyvinylpyrrolidone-mediated growth of ag nanocubes. *Nano Lett.*, 15(11):7711–7717, 2015.

[6] C. M. Wang, D. R Baer, J. E. Amonette, M. H. Engelhard, Y. Qiang, and J. Antony. Morphology and oxide shell structure of iron nanoparticles grown by sputter-gas-aggregation. *Nanotechnology*, 18(25):255603, 2007.

[7] C. M. Wang, D. R. Baer, J. E. Amonette, M. H. Engelhard, J. Antony, and Y. Qiang. Morphology and electronic structure of the oxide shell on the surface of iron nanoparticles. *J. Am. Chem. Soc.*, 131(25):8824–8832, 2009.

[8] A. Pratt, L. Lari, O. Hovorka, A. Shah, C. Woffinden, S. P. Tear, C. Binns, and R. Kröger. Enhanced oxidation of nanoparticles through strain-mediated ionic transport. *Nat. Mater.*, 13(1):26–30, 2014.

[9] L. D. Marks. Experimental studies of small particle structures. *Rep. Prog. Phys.*, 57(6):603, 1994.

[10] F. Baletto and R. Ferrando. Structural properties of nanoclusters: Energetic, thermodynamic, and kinetic effects. *Rev. Mod. Phys.*, 77:371–423, 2005.

[11] G. Wulff. Xxv. zur frage der geschwindigkeit des wachsthums und der auflösung der krystallflächen. *Z. Kristallogr. - Cryst. Mater.*, 34(1):449–530, 1901.

[12] C. Herring. *Structure and Properties of Solid Surfaces (ed. by R. Gomer and C. S. Smith)*. University of Chicago Press, 1953.

[13] T. P. Martin. Shells of atoms. *Phys. Rep.*, 273(4):199–241, 1996.

[14] G. Casillas, J. J. Velázquez-Salazar, and M. Jose-Yacaman. A new mechanism of stabilization of large decahedral nanoparticles. *J. Phys. Chem. C*, 116(15):8844–8848, 2012.

[15] A. B. Patil, D. S. Patil, and B. M. Bhanage. Selective and efficient synthesis of decahedral palladium nanoparticles and its catalytic performance for suzuki coupling reaction. *J. Mol. Catal. A-Chem.*, 365:146–153, 2012.

[16] J. B. Wu, W. P. Gao, J. G. Wen, D. J. Miller, P. Lu, J. M. Zuo, and H. Yang. Growth of au on pt icosahedral nanoparticles revealed by low-dose in situ tem. *Nano Lett.*, 15(4):2711–2715, 2015.

[17] Q. B. Zhang, J. P. Xie, J. H. Yang, and J. Y. Lee. Monodisperse icosahedral ag, au, and pd nanoparticles: size control strategy and superlattice formation. *Acs Nano*, 3(1):139–148, 2008.

[18] F. Baletto, C. Mottet, and R. Ferrando. Molecular dynamics simulations of surface diffusion and growth on silver and gold clusters. *Surf. Sci.*, 446(1):31–45, 2000.

[19] F. Baletto, C. Mottet, and R. Ferrando. Reentrant morphology transition in the growth of free silver nanoclusters. *Phys. Rev. Lett.*, 84(24):5544, 2000.

[20] D. M Wells, G. Rossi, R. Ferrando, and R. E. Palmer. Metastability of the atomic structures of size-selected gold nanoparticles. *Nanoscale*, 7(15):6498–6503, 2015.

[21] F. Baletto, C. Mottet, and R. Ferrando. Microscopic mechanisms of the growth of metastable silver icosahedra. *Phys. Rev. B*, 63(15):155408, 2001.

[22] P. Grammatikopoulos, S. Steinhauer, J. Vernieres, V. Singh, and M. Sowwan. Nanoparticle design by gas-phase synthesis. *Adv. Phys. X*, 1(1):81–100, 2016.

[23] Y. H. Xu and J. P. Wang. Direct gas-phase synthesis of heterostructured nanoparticles through phase separation and surface segregation. *Adv. Mater.*, 20(5):994–999, 2008.

[24] V. Singh, C. Cassidy, P. Grammatikopoulos, F. Djurabekova, K. Nordlund, and M. Sowwan. Heterogeneous gas-phase synthesis and molecular dynamics modeling of janus and core–satellite si–ag nanoparticles. *J. Phys. Chem. C*, 118(25):13869–13875, 2014.

[25] B. J. Alder and T. E. Wainwright. Molecular dynamics by electronic computers. Proc. Intern. Symposium on Transport Processes in Statistical Mechanics, page 97, New York, 1957. Wiley Interscience.

[26] B. J. Alder and T. E. Wainwright. Studies in molecular dynamics. i. general method. *J. Chem. Phys.*, 31(2):459, 1959.

[27] L. Verlet. Computer "experiments" on classical fluids. i. thermodynamical properties of lennard-jones molecules. *Phys. Rev.*, 159:98, 1967.

[28] C. W. Gear. *Numerical initial value problems in ordinary differential equations*. Prentice-Hall, Englewook Cliffs, NJ, USA, 1971.

[29] K. Nordlund. Molecular dynamics simulation of ion ranges in the 1 – 100 kev energy range. *Comput. Mater. Sci.*, 3:448, 1995.

[30] H. J. C. Berendsen, J. P. M. Postma, W. F. van Gunsteren, A. DiNola, and J. R. Haak. Molecular dynamics with coupling to external bath. *J. Chem. Phys.*, 81(8):3684, 1984.

[31] S. C. Harvey, R. K-Z Tan, and T. E. Cheatham. The flying ice cube: velocity rescaling in molecular dynamics leads to violation of energy equipartition. *J. Comput. Chem.*, 19(7):726–740, 1998.

[32] S. Nosé. A molecular dynamics method for simulations in the canonical ensemble. *Mol. Phys.*, 52(2):255–268, 1984.

[33] W. G. Hoover. Canonical dynamics: equilibrium phase-space distributions. *Phys. Rev. A*, 31(3):1695, 1985.

[34] H. C. Andersen. Molecular-dynamics simulations at constant pressure and-or temperature. *J. Chem. Phys.*, 72(4):2384, 1980.

[35] M. Parrinello and A. Rahman. Polymorphic transitions in single crystals: A new molecular dynamics method. *J. Appl. Phys.*, 52(12):7182, 1981.

[36] K. Nordlund, M. Ghaly, R. S. Averback, M. Caturla, T. Diaz de la Rubia, and J. Tarus. Defect production in collision cascades in elemental semiconductors and fcc metals. *Phys. Rev. B*, 57(13):7556–7570, 1998.

[37] M. Ghaly, K. Nordlund, and R. S. Averback. Molecular dynamics investigations of surface damage produced by kev self-bombardment of solids. *Phil. Mag. A*, 79(4):795, 1999.

[38] S. Plimpton. Fast parallel algorithms for short-range molecular dynamics. *J. Comput. Phys.*, 117(1):1–19, 1995.

[39] F. H. Stillinger and T. A. Weber. Computer simulation of local order in condensed phases of silicon. *Phys. Rev. B*, 31:5262, 1985.

[40] K. J. Ding and H. C. Andersen. Molecular-dynamics simulation of amorphous germanium. *Phys. Rev. B*, 34(10):6987, 1986.

[41] Z. Q. Wang and D. Stroud. Monte carlo studies of liquid semiconductor surfaces: Si and ge. *Phys. Rev. B*, 38(2):1384, 1988.

[42] N. Aichoune, V. Potin, P. Ruterana, A. Hairie, G. Nouet, and E. Paumier. An empirical potential for the calculation of the atomic structure of extended defects in wurtzite gan. *Comput. Mater. Sci.*, 17:380, 2000.

[43] A. Bere and A. Serra. Atomic structure of the dislocation cores in gan. *Phys. Rev. B*, 65:205323, 2002.

[44] J. Tersoff. New empirical approach for the structure and energy of covalent systems. *Phys. Rev. B*, 37:6991, 1988.

[45] J. Tersoff. Empirical interatomic potential for silicon with improved elastic properties. *Phys. Rev. B*, 38:9902, 1988.

[46] G. Bonny, N. Castin, and D. Terentyev. Interatomic potential for studying ageing under irradiation in stainless steels: the fenicr model alloy. *Modelling Simul. Mater. Sci. Eng.*, 21:085004, 2013.

[47] G. J. Ackland, M. I. Mendelev, D. J. Srolovitz, S. Han, and A. V. Barashev. Development of an interatomic potential for phosphorus impurities in alpha -iron. *J. Phys.-Condens. Mat.*, 16(27):S2629–42, 2004.

[48] B. J. Lee, J. H. Shim, and M. I. Baskes. Semiempirical atomic potentials for the fcc metals cu, ag, au, ni, pd, pt, al, and pb based on first and second nearest-neighbor modified embedded atom method. *Phys. Rev. B*, 68(14):144112, 2003.

[49] J. K. Chen, D. Farkas, and W. T. Reynolds. Atomistic simulation of an fcc/bcc interface in ni-cr alloys. *Acta Mater.*, 45(11):4415–4421, 1997.

[50] X. W. Zhou, H. N. G. Wadley, R. A. Johnson, D. J. Larson, N. Tabat, A. Cerezo, A. K. Petford-Long, G. D. W. Smith, P. H. Clifton, R. L. Martens, and T. F. Kelly. Atomic scale structure of sputtered metal multilayers. *Acta Mater.*, 49(19):4005–4015, 2001.

[51] A. Caro, D. A. Crowson, and M. Caro. Classic many body potential for concentrated alloys, and the inversion of order in fe-cr. *Phys. Rev. Lett.*, 95:075702, 2005.

[52] M. I. Baskes. Application of the embedded-atom method to covalent materials: A semi-empirical potential for silicon. *Phys. Rev. Lett.*, 59(23):2666, 1987.

[53] M. I. Baskes, J. S. Nelson, and A. F. Wright. Semiempirical modified embedded-atom potentials for silicon and germanium. *Phys. Rev. B*, 40(9):6085, 1989.

[54] S. M. Foiles, M. I. Baskes, and M. S. Daw. Embedded-atom-method functions for the fcc metals cu, ag, au, ni, pd, pt, and their alloys. *Phys. Rev. B*, 33(12):7983, 1986. *Erratum: ibid,* Phys. Rev. B 37, 10378 (1988).

[55] M. W. Finnis and J. E. Sinclair. A simple empirical n-body potential for transition metals. *Phil. Mag. A*, 50(1):45, 1984. *see also Erratum, ibid. 53 (1986) 161*.

[56] M. W. Finnis. *Interatomic Forces in Condensed Matter*. Oxford University Press, Oxford, 2003.

[57] M. I. Mendelev, S. Han, D. J. Srolovitz, G. J. Ackland, D. Y. Sun, and M. Asta. Development of new interatomic potentials appropriate for crystalline and liquid iron. *Philos. Mag.*, 83(35):3977–94, 2003.

[58] N. Metropolis and S. Ulam. The monte carlo method. *J. Am. Stat. Assoc.*, 44(247):335–341, 1949.

[59] N. Metropolis. The beginning of the monte carlo method. *Los Alamos Science*, 15(584):125–130, 1987.

[60] N. Metropolis, A. W. Rosenbluth, M. N. Rosenbluth, A. H. Teller, and E. Teller. Equation of state calculations by fast computing machines. *J. Chem. Phys.*, 21(6):1087, 1953.

[61] D. J. Wales and H. A. Scheraga. Global optimization of clusters, crystals and biomolecules. *Science*, 285:1368–1372, 1999.

[62] A. B. Bortz, M. H. Kalos, and J. L. Lebowitz. A new algorithm for monte carlo simulation of ising spin systems. *J. Comput. Phys.*, 17(1):10–18, 1975.

[63] V. Jansson, E. Baibuz, and F. Djurabekova. Long-term stability of cu surface nanotips. *Nanotechnology*, 27(26):265708, 2016.

[64] J. M. Jin. *The finite element method in electromagnetics*. John Wiley & Sons, 2014.

[65] R. Courant et al. Variational methods for the solution of problems of equilibrium and vibrations. *Bull. Amer. Math. Soc*, 49(1):1–23, 1943.

[66] D. Meeker. Improvised asymptotic boundary conditions for electrostatic finite elements. *IEEE T. Magn.*, 50(6):1–9, 2014.

[67] D. Meeker. Finite element method magnetics. *FEMM*, 4:32, 2010.

[68] T. F. Ciszek and G. H. Schwuttke. Method for directional solidification of silicon, January 6 1981. US Patent 4,243,471.

[69] A. Mattoni and L. Colombo. Crystallization kinetics of mixed amorphous-crystalline nanosystems. *Phys. Rev. B*, 78:075408, Aug 2008.

[70] C. Krzeminski, Q. Brulin, V. Cuny, E. Lecat, E. Lampin, and F. Cleri. Molecular dynamics simulation of the recrystallization of amorphous si layers: Comprehensive study of the ddependence of the recrystallization velocity on the interatomic potential. *J. Appl. Phys.*, 101:123506, 2007.

[71] S. M. Nakhmanson and N. Mousseau. Crystallization study of model tetrahedral semiconductors. *J.Phys.-Condens. Mat.*, 14(26):6627, 2002.

[72] S. Sastry and C. A. Angell. Liquid–liquid phase transition in supercooled silicon. *Nat. Mater.*, 2(11):739–743, 2003.

[73] P. Beaucage and N. Mousseau. Nucleation and crystallization process of silicon using the stillinger-weber potential. *Phys. Rev. B*, 71(9):094102, 2005.

[74] J. E. Jones. On the determination of molecular fields. ii. from the equation of state of a gas. *Proceedings of the Royal Society of London. Series A, Containing Papers of a Mathematical and Physical Character*, 106:463–477, 1924.

[75] J. F. Ziegler, J. P. Biersack, and U. Littmark. *The Stopping and Range of Ions in Matter*. Pergamon, New York, 1985.

[76] J. Tarus and K. Nordlund. Molecular dynamics simulation of ge surface segregation. *Thin Solid Films*, 464-465:95–98, 2003.

[77] K. Nakajima, M. Hosaka, T. Hattori, and K. Kimura. Surface segregation of ge during si growth on ge/si(001) at low temperature observed by high-resolution rbs. *Nucl. Instr. Meth. Phys. Res. B*, 190:587–591, 2002.

[78] S. M. Foiles. Calculation of the surface segregation of ni-cu alloys with the use of the embedded-atom method. *Phys. Rev. B*, 32(12):7685, 1985.

[79] A. V. Ruban, H. L. Skriver, and J. K. Nørskov. Surface segregation energies in transition-metal alloys. *Phys. Rev. B*, 59(24):15990, 1999.

[80] J. M. Cowley. An approximate theory of order in alloys. *Phys. Rev.*, 77(5):669, 1950.

[81] A. R. Tao, S. Habas, and P. D. Yang. Shape control of colloidal metal nanocrystals. *Small*, 4(3):310–325, 2008.

[82] S. M. Lee, S. N. Cho, and J. W. Cheon. Anisotropic shape control of colloidal inorganic canocrystals. *Adv. Mater.*, 15(5):441–444, 2003.

[83] V. F. Puntes, K. M. Krishnan, and A. P. Alivisatos. Colloidal nanocrystal shape and size control: the case of cobalt. *Science*, 291(5511):2115–2117, 2001.

[84] M. Grzelczak, J. Pérez-Juste, P. Mulvaney, and L. M. Liz-Marzán. Shape control in gold nanoparticle synthesis. *Chem. Soc. Rev.*, 37(9):1783–1791, 2008.

[85] T. Teranishi, R. Kurita, and M. Miyake. Shape control of pt nanoparticles. *J. Inorg. Organomet. Polym.*, 10(3):145–156, 2000.

[86] W. X. Niu, L. Zhang, and G. B. Xu. Shape-controlled synthesis of single-crystalline palladium nanocrystals. *ACS Nano*, 4(4):1987–1996, 2010.

[87] Y. J. Kang, J. B. Pyo, X. C. Ye, R. E Diaz, T. R. Gordon, E. A. Stach, and C. B. Murray. Shape-controlled synthesis of pt nanocrystals: the role of metal carbonyls. *ACS Nano*, 7(1):645–653, 2012.

[88] P. Błoński and A. Kiejna. Structural, electronic, and magnetic properties of bcc iron surfaces. *Surf. Sci.*, 601(1):123–133, 2007.

[89] M. Müller, P. Erhart, and K. Albe. Analytic bond-order potential for bcc and fcc iron—comparison with established embedded-atom method potentials. *J. Phys.: Condens. Matter*, 19(32):326220, 2007.

[90] D. T. Gillespie. Monte carlo simulation of random walks with residence time dependent transition probability rates. *J. Comput. Phys.*, 28(3):395–407, 1978.

[91] G. Wehner. Influence of the angle of incidence on sputtering yields. *J. Appl. Phys.*, 30:1762, 1959.

[92] Y. Yamamura, Y. Itikawa, and N. Itoh. Angular dependence of sputtering yields of monatomic solids. Report ippj-am-26, Institute of Plasma Physics, Nagoya University, 1983.

[93] M. P. Seah, C. A. Clifford, F. M. Green, and I. S. Gilmore. An accurate semi-empirical equation for sputtering yields i: for argon ions. *Surf. Interface Anal.*, 37(5):444–458, 2005.